

RESEARCH

LOROS: Laboratory Simulations of the Optical Radiometer composed of CHromatic Imagers (OROCHI) Experiment of the Martian Moons eXploration (MMX) Mission

Roger Stabbins* and Shingo Kameda

Abstract

The Laboratory OROCHI Simulator (LOROS) is an emulator of the Optical Radiometer composed of CHromatic Imagers (OROCHI), a multispectral and multiview imaging system for the Japan Aerospace Exploration Agency (JAXA) Martian Moons eXploration (MMX) spacecraft, that will study Phobos and Deimos with the objective of determining their origin. OROCHI consists of 8 visible/near-infrared (390–950 nm) spectral channels, hosted on 8 separate camera systems, arranged in a 3×3 grid (with an empty central site) with 10 cm spacing. Prior to completion of the OROCHI Flight Model it is important to demonstrate the ability of the cameras to resolve the subtle spectral features expected at Phobos and Deimos, and to investigate the implications of the multiview configuration when performing near-field imaging on the Phobos surface. LOROS provides a robust and portable emulator of the OROCHI Flight Model, composed of commercial off-the-shelf components and materials compliant with the ISO-6 restrictions of the JAXA Extraterrestrial Sample Curation Centre. Here we describe the configurations of the components and control software that we have developed and present the results of a series of calibration experiments, demonstrating the comparable performance of the two systems. We achieve agreement within 3% across sensor performance metrics of read noise, saturation capacity and sensitivity, and demonstrate the measurement of the reflectance of a dark diffuse reflector reference standard with a mean temporal signal-to-noise ratio of 120.

Keywords

Martian Moons eXploration, Phobos, Multispectral Imaging, Reflectance Spectroscopy

1 Introduction

Operating a new imaging system in a new environment requires preparation, but due to the development timelines and protections required of spaceflight hardware, it is rarely possible to perform extensive ground-based trials of operations and experiments with the final Flight Model of an instrument. Previous imaging teams of planetary surface imaging systems have made use of instrument emulators in laboratory and field environments (Allender et al., 2020; Cho et al., 2022; Harris et al., 2015; Martin et al., 2020) to validate the abilities of these instruments to resolve certain features of interest, to test experimental procedures and pro-

cessing pipelines, and to identify new types of data product.

Here we introduce a laboratory simulator (LOROS) for the OROCHI instrument of the forthcoming JAXA Martian Moons eXploration mission. OROCHI is a multiview multispectral imager, with the 8 spectral channels of the instrument distributed across 8 separate optical systems and sensors. This presents a unique challenge to imaging when landed on the surface of Phobos, with an expected objective distance of ~0.8 m, such that each camera will collect surface scattered light from distinct phase and emergence angles.

The purpose of LOROS is to demonstrate the ability of OROCHI to resolve changes in reflectance with 1% accuracy, requiring >100 SNR, and to investigate the impact of observing surface reflectance at distinct

*Correspondence: rstabbins@rikkyo.ac.jp

Department of Physics, Rikkyo University, 3-34-1 Nishi-Ikebukuro, Toshima, Tokyo 171-8501, Japan

Full list of author information is available at the end of the article

phase and emergence angles for each spectral channel. In this paper we introduce the LOROS system and describe the calibration of the system to validate that the performance meets the expectations of the OROCHI Flight Model.

1.1 MMX and OROCHI

The Optical Radiometer composed of CHromatic Imagers (OROCHI) instrument (Kameda et al., 2021) is a wide-angle visible-to-near-infrared (VNIR) multispectral imaging system for the Japan Aerospace Exploration Agency (JAXA) Martian Moons Exploration (MMX) mission (Kuramoto et al., 2022), with a key objective of characterising the surface spectral diversity of the moons of Mars: Phobos and Deimos. Images obtained with OROCHI whilst the MMX spacecraft is in Quasi-Satellite Orbit (QSO) will contribute to the selection of a landing site on the surface of Phobos, and, once landed at this site, further images from the surface will provide geological context for the first Phobos regolith samples to be acquired and returned to Earth, and for the operations of the MMX Rover that will be deployed on the surface (Michel et al., 2022). OROCHI will also image Deimos and the martian surface, and transient phenomena in the martian atmosphere (Ogohara et al., 2022). OROCHI complements the MMX instrument suite, that consists of high resolution cameras, a near-infrared spectrometer, a gamma-ray and neutron spectrometer, a mass spectrometer, a dust monitor, and a laser altimeter (Barucci et al., 2021; Kameda et al., 2021; Kobayashi et al., 2018; Lawrence et al., 2019; Senshu et al., 2021; Yokota et al., 2021).

1.2 Design of OROCHI

As described by Kameda et al. (2021), the performance requirements of OROCHI are driven by the mission objective of spectroscopically mapping the surface-layer distribution of hydrous minerals, and co-aligning this map with the global topography, at a resolution of less than 20 m per pixel from the QSO ‘low’ altitude of ~20 km for Phobos, and at a resolution of 100 m per pixel from the ~100 km flyby distance of Deimos. During descent to the Phobos landing site from an altitude of ~1 km a resolution of 1 m per pixel is required across a horizontal field of 50 m (at the surface), and once landed, OROCHI will be at a distance of ~0.8 m from the surface, where imaging of the sampling site is required at a resolution of 1/5 of the sample core size (<5 mm per pixel). OROCHI satisfies these requirements with a diagonal field-of-view (d-FoV) of >83°, an instantaneous field-of-view (i-FoV) of 0.44–0.46 mrad/pixel and Modulation Transfer Function (MTF) of >0.3 for 480–860 nm and >0.2 at 390 and

950 nm at the sensor Nyquist frequency of 91 lp/mm. Resolving the ~3–4% band-depth of hydrous minerals requires a signal-to-noise ratio (SNR) of ≥100 (Cloutis et al., 2011).

OROCHI is composed of 8 cameras, each with a separate optical path and 8 megapixel (MP) CCD (Charge-Coupled Device) detector, distributed in a grid, with a separation of 100 mm between neighbouring cameras. The 7 multispectral bands of 390 ± 25 nm, 480 ± 15 nm, 550 ± 15 nm, 650 ± 20 nm, 730 ± 20 nm, 860 ± 20 nm and 950 ± 30 nm (central wavelength±half-width-at-half-maximum) were selected to complement the observations of asteroid Ryugu made by the Optical Navigation Camera Telescope (ONC-T) of the Hayabusa2 spacecraft (Kameda et al., 2017), and for measurement of the ~650 nm absorption feature of the red unit of Phobos (Fraeman et al., 2014). The 7 multispectral bands have focus optimised for orbital observations, and an 8th monochromatic channel, that duplicates the 550 nm channel, is optimised for the 0.8 m imaging distance at the surface.

1.3 Motivation for LOROS: the Laboratory OROCHI Simulator

Prior to the arrival of MMX at the Mars system it is important to develop and demonstrate the image capture and processing routines for this new multispectral imaging system, to ensure performance requirements are met, and to prepare for efficient operation and analysis during the mission. The Laboratory OROCHI Simulator (LOROS) has been developed for this purpose, prior to the delivery of the Flight and Engineering Models of OROCHI. LOROS will be used to image a sample of a carbonaceous chondrite, representative of the anticipated Phobos surface composition and physical properties, including representation of the hydrous absorption feature that OROCHI will seek to map (Cloutis et al., 2011), and samples of C-type asteroid Ryugu (Nakamura et al., 2022), that represent pristine asteroid material prior to contamination by the Earth environment. We will also use LOROS to image samples of B-type asteroid Bennu to investigate the differences and similarities between Ryugu and Bennu, as reported from remote sensing and analytical sample analysis (Hamilton et al., 2024; Lauretta et al., 2022; Yumoto et al., 2024). In this paper, we describe the LOROS facility in detail, including calibration of the system and configuration for matching the expected performance of OROCHI, in preparation for these imaging experiments.

2 LOROS

In this section we describe the design of LOROS in relation to the expected performance of OROCHI, and

introduce the terms used for comparing the systems, pertaining to the spatial sampling, sensor response, and spectral sampling of reflectance.

2.1 LOROS Design Overview

Like OROCHI, LOROS is composed of 8 spectral channels hosted by 8 separate camera systems, mounted with parallel optical axes on a 3-tier optical bench, with orthogonal separations of 10 cm. Each channel hosts a bandpass spectral filter, with the placements matching the planned arrangement of the OROCHI Flight Model, as illustrated in figure 1. LOROS is mounted with all co-planar image planes in the horizontal, with the object plane positioned at 80 cm in front of the optical bench to match the imaging geometry of the MMX spacecraft when landed on the surface of Phobos.

The object plane is directly illuminated by a 150 W halogen lamp (Hayashi-Repic LA-150UE) with high stability (intensity variation of $< \pm 0.5\%$ over 25-hour cycle (Cho et al., 2022)) focused with a 50 mm F/1.9 lens (Kowa LM-50-IR), positioned with a nominal incidence angle of 30° , and an object distance of $\sim 10\text{--}40$ cm, depending on the experiment. An additional aperture mounted to the lamp fibre optic cable allowed for precise adjustment of the object-plane projected lamp beam diameter from $\sim 5\text{--}50$ mm.

The LOROS system is hosted on an aluminium frame such that the camera locations relative to the sample area are kept rigid. The frame was designed to be dismantled into two parts, such that the system could be transported through the airlock of the Extraterrestrial Sample Curation Centre (ESCuC) at the JAXA Institute of Space & Astronautical Science (Sagamihara). We fitted multiple layers of dark cloth to the frame to isolate the cameras and experiment area from ambient lighting, and to minimise stray light contributions. The dark cloth and all other materials used in the frame were selected for compliance with the ESCuC ISO-6 Clean-room status.

2.2 LOROS Sensor Characteristics and Configuration

Each channel of LOROS uses a SonyTM CMOS (Complementary Metal-Oxide-Semiconductor) PreguisTM IMX249 sensor (Sony Corporation, 2015), hosted in a Commercial Off-the-Shelf (COTS) DMK 33GX249 Monochrome Industrial Camera with a GigE Interface (The Imaging Source Europe GmbH., 2019). The IMX249 sensor was selected for LOROS to approximate the performance of the OnSemiTM KAI-08051 CCD sensor that will be used for OROCHI (as described by Kameda et al. (2021)) that was selected to fulfil the MTF, SNR and FoV design requirements described above. The expected characteristics of the sensors as reported in the publicly available KAI-08051

datasheet (OnSemi., 2015), and as reported by users of the IMX249 in the literature (Baumer Optronic GmbH., 2017; Grøtte et al., 2022) are given in table 3, alongside the expected characteristics of the IMX249 as configured for LOROS, and the measured characteristics for each channel of LOROS, as described in the method and results sections. The key differences are as follows.

2.2.1 Sensor Format

The IMX249 (LOROS) is a 1/1.2" format (13.4 mm diagonal) 2.35 MP sensor with $5.86\text{ }\mu\text{m}$ pitch, whilst the KAI-08051 (OROCHI) is a 4/3" format (22.66 mm diagonal) 8 MP sensor with $5.5\text{ }\mu\text{m}$ pitch. The approximately equal pixel pitch of the sensors supports the use of equivalent system optics, with Nyquist frequencies of 85.3 lp/mm for the IMX249 in comparison to 90.9 lp/mm for the KAI-08051, such that the choice of the IMX249 for LOROS affords a spatial resolution that approximately matches OROCHI. The smaller format of the IMX249 restricts LOROS experiments to use only the central $\sim 56^\circ$ d-FoV of each channel, a sub-frame of the OROCHI $\sim 83^\circ$ d-FoV. This sub-framing does not affect the planned near-field experiments (object distance ~ 0.8 m), as the area of the sample illuminated by the lamp configuration is $\sim 3^\circ$ of the field.

2.2.2 Sensor Radiometric Performance

OROCHI will use a 14-bit Analog-to-Digital Converter (ADC) with the KAI-08051, but the IMX249 is limited to 12-bit operation. However, as the effective dynamic range¹ of the KAI-08051 is ~ 11.0 -bit, the performance of the sensor can be well-approximated with the 12-bit depth of the IMX249, that has an effective dynamic range of ~ 12.2 -bits. The expected sensitivity of the KAI-08051 when down-sampled to 12-bit resolution is $4.88\text{ e}^-/\text{DN}$ (computed from OnSemi. (2015)), which exceeds the expected IMX249 sensitivity of $7.98\text{ e}^-/\text{DN}$. To match the performance, we apply the quantised gain setting corresponding to a gain of 4.3 dB to the IMX249, bringing the expected sensitivity to $4.86\text{ e}^-/\text{DN}$. The application of this gain effectively clips the saturation capacity of the IMX249 at $\sim 19500\text{ e}^-$, bringing the maximum achievable Signal-to-Noise Ratio (SNR_{Max}) of the system to ~ 139.6 , slight less ($\sim 1\%$) than the KAI-08051 SNR_{Max} of 141.4 (via full well capacity of 20000 e⁻). This tuning of sensor gain has the effect of tuning the relationship between Digital Number and Signal-to-Noise Ratio of LOROS to match that of a 12-bit equivalent of OROCHI.

2.2.3 Spectral Sensitivity and Expected Dark Signal

The quantum efficiency (QE) of the IMX249 is greater than the KAI-08051, with values of $\sim 77\%$ and $\sim 8\%$

vs. $\sim 49\%$ and $\sim 2\%$ at 500 nm and 950 nm respectively (OnSemi., 2015; The Imaging Source Europe GmbH., 2019). However, the spectral power distribution of the illumination approximately compensates for the differences in spectral sensitivity, such that the at-sensor irradiance for each LOROS channel is comparable to that expected for OROCHI at Phobos. The dark signal expected for the IMX249 is approximately double that of the KAI-08051, but for the expected exposure regimes of < 1 s when imaging low albedo samples (of $\lesssim 7\%$ reflectance), we expect the total dark signal to be negligible (< 1 DN).

2.2.4 Sensor Architecture

The IMX249 is a CMOS architecture sensor, whereas the KAI-08051 is a CCD. Functionally, CMOS architectures may introduce nonlinearity in the detector response, and follow exposure and readout procedures that differ from a CCD. These do not affect the scope of the studies conducted here, as we assume a stationary target relative to the exposure duration, and the literature reports that the nonlinearity error of the IMX249 is as low as 0.37% (Baumer Optronic GmbH., 2017), in comparison to 1% reported for the KAI-08051 (OnSemi., 2015).

2.3 LOROS Optical Characteristics and Configuration

2.3.1 Lenses

The focal lengths of the individual channels of OROCHI are in the range of 13.23–13.57 mm, with apertures in the range of F/5.8–F/6.4, with the values for each channel optimised for the given central wavelength and fixed (Kameda et al., 2021). We emulate the OROCHI lenses with adjustable 12.5 mm F/1.4 lenses (Kowa LM12HC), capable of achieving resolution of 160 lp/mm (Kowa Optimed Deutschland GmbH., 2014), and set the apertures manually to match those of OROCHI (see method section). The lens datasheet gives an expected MTF of > 0.45 in the range of 85–91 lp/mm over 436–656 nm (Kowa Optimed Deutschland GmbH., 2014), giving a small margin over the OROCHI requirement of MTF > 0.3 at the sensor Nyquist. For this study we have set the focus of all channels to 0.8 m (see method discussion). As discussed above, the smaller sensor format of the IMX249 limits the d-FoV of LOROS to $\sim 56^\circ$. The slightly shorter focal length and slightly larger pixel pitch of the IMX249 results in an expected i-FoV of LOROS of 0.43 mrad/pixel, slightly exceeding the expected OROCHI minimum resolution of 0.40 mrad/pixel, but satisfying the 0.5 mrad/pixel requirement defined by Kameda et al. (2021).

2.3.2 Spectral Filters

The lens of each spectral channel is fitted with a hard-coated OD 4.0 thin-film interference filter (Edmund Optics), mounted in front of the lens first surface. Representative filters with central wavelength (CWL, λ_c) and full-width-at-half-maximum (FWHM, $\Delta\lambda$) were selected from the manufacturer catalogue that matched within 10 nm of those of OROCHI. The apertures, CWLs and FWHMs of the channels are presented in table 1. As an exception, for the 650 nm channel a FWHM of 10 nm was chosen, that at the time of selection matched the planned characteristics of the OROCHI 650 nm channel, that has since been extended to a 40 nm FWHM.

3 Methods

In this paper we characterise the performance of LOROS so that experiments performed with the facility can be directly compared to in-flight experiments performed with OROCHI at the martian moon system. We perform this characterisation by deriving the MTF and SNR of each spectral channel by measuring the knife-edge line-spread function and photon-transfer curve (Janesick et al., 1985). We also demonstrate the measurement of reflectance by computational resampling of a high-resolution reflectance spectrum of a carbonaceous chondrite, and empirically by imaging a reflectance standard calibration target, and by recording the signal-to-noise ratio of this recovered reflectance.

3.1 Camera Configuration

Prior to characterisation, we configured the camera firmware and control software to the appropriate gain and offset levels, and for 12-bit image readout, and performed a series of tuning operations to set the focus and aperture of each spectral channel.

The Python interface for controlling the DMK 33GX249, provided by The Imaging Source™ (TIS), allows for discrete remote gain control, that we set to 4.30 dB to achieve an expected sensitivity of 4.86 e⁻/DN. We configured the DMK 33GX249 for 12-bit output via the Python TIS interface, by setting video and sink formats to ‘Y16’, combining the 2 bytes of each pixel to a 16-bit unsigned integer image, and scaling by 1/16 to give 12-bit integer pixel values. The interface allows for black-level (or brightness) adjustment, that we set to 4 DN, after establishing that the observed read noise (derived from the standard deviation of repeat dark frame images captured in the range of 6 μ s–3 s) did not change for black-level values greater than this, implying that 4 DN was the minimum black-level required to avoid underflow. We included in our Python control library a function for

changing the frame rate of the readout, such that for exposures less than 0.5 s the Frame Rate was set to 30 frames per second (fps), and 1 fps otherwise. We performed a series of tests under a variety of frame rates to establish that this configuration rule provided the most stable sensor response over the entire range of exposure times. We implemented an auto-exposure algorithm in the Python control library, that follows the percentile-style algorithm described by Maki et al. (2003). The algorithm finds the exposure value that produces an image with a defined number of pixels allowed to exceed a defined percentage of the camera sensor range within a defined tolerance, and optionally over a defined region of interest.

We focused each channel lens under conditions of maximum aperture diameter ($F/1.4$, for minimum depth-of-field) with a 36-spoke Siemens Star chart (Thorlabs R1L1S2P) in the sample position of the object plane (0.8 m) under lamp illumination, and adjusted the focus manually to minimise the radius of optical blur in the chart image for each channel.

We tuned the aperture of each channel to achieve the given target F-number ($f\#_t$) with a manual and iterative process, by comparing the exposure times required to capture statistically identical images at the adjusted aperture and a reference $F/1.4$ aperture. To do this, we found the calibration exposure time t_c required to image a reflectance standard with $F/1.4$ such that ≤ 10 pixels exceeded a target level of 3275 DN (80% of the response range) via the auto-exposure routine, and then by computing a target exposure time t_t that would be satisfied by the required aperture value $f\#_t$ according to $t_t = t_c * f\#_t / 1.4^2$. We adjusted the aperture manually, re-executed the auto-exposure routine and compared the output exposure time with t_t , and repeated this iteratively until the target exposure was satisfied within an absolute tolerance of 2.5%. We used a 5% reflectance Spectralon calibration standard, illuminated in the sample zone with nonuniformity in the sample region-of-interest zone of $\leq 4.5\%$. We validated the method by also computing the expected target level (DN) of the reflectance standard when imaged with an exposure time of t_c under the target aperture value, and by comparing this to the mean of 25 repeated images captured at t_c under the final aperture.

3.2 Spatial Sampling

To characterise the spatial sampling we measured the MTF of each channel by imaging a slant-edge, and extracted the line-spread function, using industry standard open-source software MTF-Mapper (van den Bergh, 2023). We oriented the slant-edge, a back-illuminated razorblade, at an apparent² angle of $\sim 7^\circ - 8.5^\circ$ to the vertical, placed in the object plane (at

0.8 m) crossing the centre of the sample region, with back-illumination provided by the halogen lamp reflected diffusely from white paper placed ~ 4 cm behind the blade, with the lamp oriented such that the near face of the blade received no illumination. We captured 25 repeat illuminated images and 25 dark frames at matching exposure times, for each spectral channel, and, after dark subtraction, flat-fielding and image averaging and down-sampling to 8-bit depth greyscale values, we used the MTF-mapper software to derive the line-spread function and MTF from a 40×40 pixel region of interest. The slant-edge method and MTF-Mapper processing generates plots of contrast against spatial frequency (line-pairs per mm), from which we record the contrast at the sensor Nyquist frequency, of 85.3 lp/mm ($MTF_{Nyq.}$), for comparison against the expected MTF at the OROCHI sensor Nyquist frequency. We repeated the measurement 5 times with the knife-edge randomly re-oriented, within the range of $\sim 5^\circ - 10^\circ$, and took the average and standard deviation of $MTF_{Nyq.}$ over these readings.

3.3 Sensor Response

To characterise the sensor performance across the digital signal range we measured the sensor noise as a function of signal, by capturing sequences of images of uniform illumination across the sample region at increasing exposure durations, and by capturing accompanying images with the same sequence of exposures in the absence of illumination (dark frames). From these observations we derived for each spectral channel, following the photon-transfer method (Janesick et al., 1985) and EMVA 1288 standard (Jähne, 2016), measures of the saturation capacity, linearity error, read noise, dark current, sensitivity, maximum SNR, dynamic range and fixed-pattern noise, and we fitted a linearity correction model. We also measured the digital flux of each channel to compare the LOROS illumination conditions to those expected for OROCHI at Phobos.

We performed four sequences of illuminated image capture, labelled F*S99L10, F*S5L10, FGS99L10 and FGS99L2. We performed two sequences (F*S99L10, F*S5L10) with all filters mounted to the cameras, using two 1.25" diameter Spectralon™ diffuse reflectance standards, of 99% and 5% reflectance, referred to from herein as SCT99 and SCT5 respectively, to investigate the instrument response over two different intensity, and therefore exposure, regimes, and at the designated spectral band of each camera, at fixed illumination brightness (lamp setting of 10 arbitrary units). We then performed two sequences (FGS99L10 and FGS99L2) imaging SCT99, with the filters removed and all apertures reduced to $F/16$, and the

550 nm (green) filter mounted on the lamp lens, with the lamp at two brightness settings, 10 and 2, to investigate the wavelength independent instrument response over two different intensity regimes. In this second sequence set we increased the sampling density over exposure.

For each sequence we positioned the reflectance standard at a 0.8 m object distance in the centre of the sample region, under 30° incidence lamp illumination. We selected a 28×28 ($M \times N$) pixel region of interest (ROI) in each channel to treat as the uniformly illuminated sensor area, and we tuned the lamp lens to minimise the spatial nonuniformity over this region, to $\lesssim 2\%$ for SCT99 and $\lesssim 5\%$ for SCT5 in each channel (EMVA 1288 recommends $<3\%$).

For each step of the imaging sequence we increased the exposure by a factor of $\times 1.2$ for F*S99L10 and F*S5L10, and by $\times 1.05$ for FGS99L10 and FGS99L2, with an initial exposure of $t_{exp} = 6 \mu s$, until the mean signal over the ROI reached 99% of the maximum signal ($S_{Max} = 2^{12} - 1$) (approximating complete image saturation), after which we reduced the exposure by a factor of $\times 0.99$, and continued the sequence until the mean signal was reduced to 80% of S_{Max} . This procedure ensured dense data collection in the region of the sensor saturation capacity. At each exposure we captured 2 identical illuminated images ($\mathbf{S}_1, \mathbf{S}_2$) and 25 dark images (\mathbf{D}_i). We averaged the 25 repeat dark images for each exposure to provide dark signal bias frames with suppressed dark-shot and read noise (eq. 1), and subtracted these from the illuminated frames (of corresponding exposure) to give above-bias signal images.

$$\bar{\mathbf{D}} = \frac{1}{25} \sum_{i=0}^{i=24} \mathbf{D}_i \quad (1)$$

We computed the mean signal μ_S DN (eq. 2) and standard deviation σ_T DN (eq. 3) from the above-bias signal image pairs (4), and computed the mean-square difference between the illuminated image pairs (scaled by $1/\sqrt{2}$) to estimate the combined read and shot noise σ_{rs} DN (eq. 5) by suppressing fixed-pattern noise.

$$\mu_S = \frac{1}{MN} \sum_i^{MN} (\mathbf{S}_1[i] - \bar{\mathbf{D}}[i]) \quad (2)$$

$$\sigma_T = \left(\frac{1}{MN} \sum_i^{MN} |(\mathbf{S}_1[i] - \bar{\mathbf{D}}[i]) - \mu_S|^2 \right)^{\frac{1}{2}} \quad (3)$$

$$\mathbf{S}_p = (\mathbf{S}_1[i] - \bar{\mathbf{D}}[i]) - (\mathbf{S}_2[i] - \bar{\mathbf{D}}[i]) \quad (4)$$

$$\sigma_{rs} = \left(\frac{1}{2MN} \sum_i^{MN} |\mathbf{S}_p - \langle \mathbf{S}_p \rangle|^2 \right)^{\frac{1}{2}} \quad (5)$$

After performing this processing on the image pairs and dark frames for each exposure, we obtained vectors indexed by exposure step $k \in [0, N_{exp}]$ ($t_{exp}[k], \mu_S[k], \sigma_T[k], \sigma_{rs}[k]$), that we refer to as photon-transfer data. We repeated this sequence of increasing exposure under dark conditions, with the sequence terminating at a maximum exposure of 50 s (under the assumption that saturation would not be reached) to provide data for deriving the read noise and dark current. The mean dark signal (μ_D DN), total noise (σ_{D-T} DN) and read + shot noise (σ_{D+rs} DN) were similarly computed, and aggregated into vectors indexed by k , that we refer to as dark-transfer data. We repeated this sequence for each camera, and for each of the F*S99L10, F*S5L10, FGS99L10 and FGS99L2 experiments. We note that due to the different spectral sensitivity and illuminant spectral power distribution across each channel, target and lamp brightness, a different number of exposures (N_{exp}) were used for each channel and experiment, in the range of ~ 20 –220.

In the following we discuss the key performance metrics from the derived signal and noise results that we computed for each camera and experiment.

3.3.1 Saturation Capacity

The saturation capacity defines the largest observable mean value that is not biased by saturated pixels. Saturated above-mean pixel values may be incurred in the ideal case due to photo-response non-uniformity (PRNU) and shot-noise, but in practice spatial nonuniformity of the illumination across the sensor can also contribute. We measured the saturation capacity ($\mu_{S,sat}$ DN) by taking the value $\mu_S[k]$ for the exposure index k at which the maximum value of $\sigma_T[k]$ occurred (eqs. 6, 7).

$$k_m = \arg \max_k (\sigma_T[k]) \quad (6)$$

$$\mu_{S,sat} = \mu_S[k_m] \quad (7)$$

We computed values for the estimated saturation capacity ($\tilde{\mu}_{S,sat}$) by scaling S_{Max} under the assumption of a maximum above-mean pixel value of 3σ , with $\sigma = \text{PRNU}$, by equation 8.

$$\tilde{\mu}_{S.\text{sat}} = \frac{S_{\text{Max}}}{1 + 3\text{PRNU}} \quad (8)$$

As we expect spatial nonuniformity in our illumination source, we also compute the estimated effective full-well capacity of each LOROS camera with equation 9, for direct comparison with the expected full-well capacity of OROCHI, the expected full-well capacity of the 0.0 dB gain configuration of LOROS, and the expected *effective* full-well capacity of LOROS after application of the 4.30 dB gain.

$$\tilde{n}_{FW} = \frac{S_{\text{Max}}}{K} \quad (9)$$

3.3.2 Linearity Error and Digital Flux

We measured the linearity error (LE %) of each channel by performing linear least squares fitting of $\mu_S[k]$ to $t_{exp}[k]$ for $\mu_S \in [0.05\mu_{S.\text{sat}}, 0.95\mu_{S.\text{sat}}]$, weighted by $1/\mu_S^2$, yielding slope and offset values m and c . We computed the deviation from linearity with

$$\varepsilon[k] = 100 \frac{\mu_S[k] - (m\mu_S[k] + c)}{m\mu_S[k] + c} \quad (10)$$

We report the mean of $\varepsilon[k]$ as LE (%). To estimate the illumination with respect to the expected imaging conditions of OROCHI at Phobos, we interpreted the slope coefficient of the linear fit m as the digital flux Φ DN/s.

3.3.3 Linearity Correction Model

We fitted a quadratic model to $\varepsilon[k]$ against μ_S in the range of $\mu_S \in [0.05\mu_{S.\text{sat}}, 0.95\mu_{S.\text{sat}}]$ to give the function $\varepsilon(S)$ (eq. 11).

$$\varepsilon(S) = nl_0 + nl_1S + nl_2S^2 \quad (11)$$

For a given pixel level S DN, we can correct for non-linearity by performing the correction given by

$$g(S) = \frac{S}{(1 + \varepsilon(S)/100)} \quad (12)$$

where $g(S)$ is the linearised pixel value.

3.3.4 Read Noise, Bias and Dark Current

We measured the read noise (σ_r DN), bias (b DN) and dark current (Φ_D DN/s) from the dark-transfer data. We performed linear least squares fitting of $\sigma_{D-rs}[k]^2$ to $t_{exp}[k]$, weighted by $1/\sigma_{D-rs}[k]^4$, yielding σ_r as the square root of the intercept. We performed linear least squares fitting of μ_D to t_{exp} , yielding b as the intercept and Φ_D as the slope.

3.3.5 Sensitivity

We measured the sensitivity (K e⁻/DN) first as a function of μ_S as

$$K[k] = \frac{\mu_S[k]}{\sigma_s[k]^2} \quad (13)$$

where σ_s is the shot-limited data, computed by removal of the read noise by $\sigma_s^2 = \sigma_{rs}^2 - \sigma_r^2$, and then obtained a mean value of K over the range of $k : \mu_S[k] \in [0.05\mu_{S.\text{sat}}, 0.95\mu_{S.\text{sat}}]$.

3.3.6 Maximum SNR and Dynamic Range

Using K we converted all derived metrics from DN to e⁻ based units, and computed the maximum signal-to-noise ratio (SNR_{Max}) as

$$\text{SNR}_{\text{Max}} = \sqrt{\mu_{e.\text{sat}}} \quad (14)$$

and the dynamic range (DR) as

$$\text{DR} = \frac{\mu_{e.\text{sat}}}{\sigma_{e.r}} \quad (15)$$

(the ratio of the saturation capacity to read noise in electron units). We also computed the shot-limited SNR as a function of signal with

$$\text{SNR}[k] = \frac{\mu_S[k]}{\sigma_s[k]} \quad (16)$$

3.3.7 Flat-Fields, PRNU and DSNU

We performed flat-field calibration of each camera across each filter profile with the lens and filter removed, such that only the sensor PRNU contributed to the measurement. This neglected the fixed pattern noise associated with the illumination, lens and filters, that we would expect to change as the filters and illumination were adjusted for various experiments. With the lens (and filters) removed from all cameras, we illuminated the SCT99 target in the sample area, and repeated the flat-field measurements with each of the

filters mounted to the lamp lens, to obtain 7 flat-field frames for each of the 8 cameras. We adjusted the target position such that all sensors were approximately uniformly illuminated, and captured 36 repeat exposures for each camera, such that the image median was 50% of the digital signal range (2048 DN), and averaged these to suppress random noise, to give the frame $\bar{\mathbf{S}}_{y,50}$. We then captured 36 repeat dark exposures at the same exposure values, and averaged these and subtracted from $\bar{\mathbf{S}}_{y,50}$ to remove dark signal and bias. To remove low-frequency variations in illumination across the field of each sensor, we normalised the flat-field image to a copy of itself (denoted $\tilde{\mathbf{S}}_{y,50}$) that we smoothed with a two-pass filtering process: first, a 31×31 pixel median filter, then a 64×64 pixel Gaussian filter. We used this normalised image as the final flat-field \mathbf{F} , for each camera and at each wavelength. We computed the PRNU using the standard deviation σ_F and mean μ_F of \mathbf{F} over the same ROI used for the photon-transfer experiment, as $\text{PRNU} = 100 \times \sigma_F / \mu_F$. We used the dark frames to measure the Dark Signal Non-Uniformity (DSNU) by taking the standard deviation across the ROI used ($\text{DSNU} = \sigma_d$).

3.4 Reflectance Simulations

To illustrate the implications of the spectral and radiometric sampling of LOROS in comparison to OROCHI, we performed spectral resampling (eq. 17) of a high-resolution ($\delta\lambda = 1 \text{ nm}$) spectral reflectance profile ($R(\lambda)$) of a CM2 Chondrite, Nogoya, and the manufacturer supplied reflectance profile for the SCT5 target, with top-hat approximations of the filter transmission profiles ($T(\lambda|\lambda_c, \Delta\lambda)$), to give the expected reflectance for each filter ($R[\lambda_c]$).

$$R[\lambda_c] = \frac{\int R(\lambda)T(\lambda|\lambda_c, \Delta\lambda)d\lambda}{\int T(\lambda|\lambda_c, \Delta\lambda)d\lambda} \quad (17)$$

We performed repeat sampling ($N=100$) with additive Gaussian noise, drawn from a distribution with standard deviation computed from the required SNR of 100 (eq. 18).

$$\epsilon_i \sim \mathcal{N}\left(0, \left(\frac{R[\lambda_c]}{\text{SNR}}\right)^2\right) \quad (18)$$

$$R_i[\lambda_c] = R[\lambda_c] + \epsilon_i \quad (19)$$

We sourced the spectral reflectance data from the University of Winnipeg Spectrometer Facility (Cloutis, 2015; Cloutis et al., 2006) via the Western Washington

University Visible-Infrared Spectral Browser: VISOR (St. Clair and Million, 2022), using sample ID MJG 011_0_230 (Nogoya).

We simulated the measurement of the $0.7 \mu\text{m}$ hydration-correlated absorption feature by computing the $\lambda_{bc}=725 \text{ nm}$ band-depth (730 nm for OROCHI) between the $\lambda_{sw}=550 \text{ nm}$ and $\lambda_{lw}=850 \text{ nm}$ (860 nm for OROCHI) band shoulders (eq. 20), following the method demonstrated by Kameda et al. (2015).

$$\text{BD}\lambda_{bc}^{\lambda_{lw}} = 1 - \frac{R[\lambda_{bc}]}{aR[\lambda_{sw}] + bR[\lambda_{lw}]} \quad (20)$$

$$a = 1 - b \quad (21)$$

$$b = \frac{\lambda_{bc} - \lambda_{sw}}{\lambda_{lw} - \lambda_{sw}} \quad (22)$$

We repeated the simulation for all noise-added reflectance samples, and reported the mean μ_{BD} and standard deviation σ_{BD} of the band-depth across the distribution, and the associated signal-to-noise ratio $\text{SNR}_{BD} = \mu_{BD} / \sigma_{BD}$.

3.5 Reflectance Measurements

To characterise the ability of LOROS to recover the spectral reflectance profile of an illuminated sample, we imaged the SCT5 and SCT99 targets, and used the SCT99 images and manufacturer supplied reference reflectance spectrum to calibrate the SCT5 images into units of reflectance factor. We then compared the recovered SCT5 reflectance to the manufacturer supplied reference reflectance spectrum, to validate the complete reflectance factor measurement process. We chose the SCT5 target as a material with reflectance representative of the low albedo ($\sim 1\%$) of Phobos (Fraeman et al., 2012), but with well characterised and approximately spatially homogenous reflectance.

We computed the SCT5 reflectance factor image $\mathbf{R}_5[\lambda_c]$ of the spectral channel of centre-wavelength λ_c by eq. 23,

$$\mathbf{R}_5[\lambda_c] = \frac{\Phi_5[\lambda_c]}{\Phi_{99}[\lambda_c]} R_{99}[\lambda_c] \quad (23)$$

where $\Phi_5[\lambda]$ and $\Phi_{99}[\lambda]$ represent the outgoing flux from the SCT5 and SCT99 samples, imaged under identical illumination and observation geometries, and $R_{99}[\lambda]$ is the reflectance of SCT99 over the transmission profile of the filter with CWL of λ_c . We estimated $R_{99}[\lambda_c]$ about the filter CWL and FWHM with eq. 17, using the manufacturer supplied high-resolution ($\delta\lambda = 1 \text{ nm}$) reflectance spectrum calibration data $R_{99}(\lambda)$, which also gives associated uncertainty $\sigma_{R_{99}}(\lambda)$ for

each data point. We note that this observation of reflectance factor (ratio of flux emitted from the sample to that of a perfect Lambertian reflector under identical illumination and observation geometries) differs from the radiance factor (ratio of flux emitted from the sample to normal-incident Solar irradiance) that OROCHI will observe at Phobos, but serves as an experimentally convenient proxy that reduces the uncertainty that would be introduced through radiometric calibration of the illumination source.

We represented the flux images $\Phi_5[\lambda_c]$ and $\bar{\Phi}_{99}[\lambda_c]$ in units of digital flux DN/s, that we derived from the digital intensity images, $\mathbf{S}_5[\lambda_c]$ and $\bar{\mathbf{S}}_{99}[\lambda_c]$, after flat-fielding, against flat-field $\mathbf{F}[\lambda_c]$, and dark subtraction, against dark frames $\bar{\mathbf{D}}_5[\lambda_c]$ and $\bar{\mathbf{D}}_{99}[\lambda_c]$, linearisation by eq. 12, and exposure correction against exposure times t_5 and t_{99} . The bar (\bar{X}) denotes that these digital intensity images have been averaged over a set of repeat images, to suppress random noise. Given that the purpose of our investigation is to demonstrate equivalent performance of LOROS with OROCHI, we limited ourselves to considering single-frame exposures only of SCT5, as will be the in-flight operational constraints of OROCHI. To minimise uncertainty associated with the reflectance calibration and dark subtraction we captured $n_{99} = 25$ repeat frames of SCT99, and $n_d = 25$ repeat dark frames, for each channel, where each dark frame was captured with the same exposure as the associated illuminated frame. To measure the noise of LOROS empirically we captured $n_5 = 25$ repeat images of SCT5, and computed the root-mean-square error (RMSE), that we estimated with the standard deviation of the pixel values over the repeat frames (see 3.6). The conversion is given by equations 24 and 25

$$\bar{\Phi}_{99}[\lambda_c] = \frac{1}{t_{99}[\lambda_c]} \mathbf{F}[\lambda_c] g (\bar{\mathbf{S}}_{99}[\lambda_c] - \bar{\mathbf{D}}_{99}[\lambda_c]) \quad (24)$$

$$\Phi_5[\lambda_c] = \frac{1}{t_5[\lambda_c]} \mathbf{F}[\lambda_c] g (\mathbf{S}_5[\lambda_c] - \bar{\mathbf{D}}_5[\lambda_c]) \quad (25)$$

To optimise the signal-to-noise ratio for each channel, whilst avoiding pixel saturation and breakdown of linearity, we found exposure values for $t_5[\lambda_c]$ and $t_{99}[\lambda_c]$ by performing auto-exposure under the condition that ≤ 10 pixels over a 40×40 ROI centred on the centre of the target disc exceeded 85% of the sensor range (3481 DN). We performed this auto-exposure independently for each camera, and for each target.

Note that equation 23 produces a reflectance image, with an independent reflectance value for each pixel.

This accounts for the spatial inhomogeneity of the projection of the illumination over the sample area. High-frequency spatial variations caused by the lamp fibre-optic pattern were mitigated by defocusing of the lens, but vignetting could not be removed. The lamp illumination was fixed and untouched for both SCT5 and SCT99 imaging sequences, and the object distances of the target surfaces were made equal, such that the illumination on the target surface sampled by a given pixel for both imaging sequences could be assumed to be constant.

We computed the final reported reflectance by averaging over a 20×20 ROI centred on the SCT5 disc centre in each channel, to give $\mu_{R_5}[\lambda_c]$:

$$\mu_{R_5}[\lambda_c] = \frac{1}{20 \times 20} \sum_{i \in ROI} \mathbf{R}_5[\lambda_c][i] \quad (26)$$

We can compare our observed reflectance $\mu_{R_5}[\lambda_c]$ to the values derived from the manufacturer supplied reflectance of SCT5, $R[\lambda_c]$ (eq. 17). However, the manufacturer supplied reflectance was observed under an $8^\circ/H$ observation geometry³, approximating directional-hemispherical albedo, whereas LOROS effectively observes the directional-directional albedo for 30° incident illumination, at emergence angles of $\sim 7.1^\circ$ and $\sim 10.0^\circ$ (across azimuth angles of $0-315^\circ$). As SCT5 is not expected to be a perfect isotropic reflector, we anticipate some small difference between the reference and the observed reflectance. To correct for this, we compare the normalised reflectance factors of the observed and reference reflectance, normalised to the 550 nm channel, denoted $N_{\mu_{R_5}}^{550}[\lambda_c]$ and $N_{R_5}^{550}[\lambda_c]$ respectively (eqs. 28 & 27).

$$N_{R_5}^{550}[\lambda_c] = \frac{R_5[\lambda_c]}{R_5[550]} \quad (27)$$

$$N_{\mu_{R_5}}^{550}[\lambda_c] = \frac{\mu_{R_5}[\lambda_c]}{\mu_{R_5}[550]} \quad (28)$$

3.6 Uncertainty Quantification and SNR

We report the uncertainty on $\mu_{R_5}[\lambda_c]$ in 2 ways: as the standard deviation of $\mathbf{R}_5[\lambda_c]$ over the ROI ($s_{R_5}[\lambda_c]$), and as the mean of the RMSE over the ROI ($\mu_{\sigma_{R_5}}[\lambda_c]$).

$s_{R_5}[\lambda_c]$ (eq. 29) captures the dispersion of pixel reflectance values about the mean value, due to the spatial inhomogeneity of the sampled area, residual fixed pattern noise of the camera (remaining after flat-fielding and dark frame subtraction), and random noise over the $N_R = 20 \times 20$ pixels.

$$s_{R_5}[\lambda_c] = \left(\frac{1}{N_R} \sum_{i \in ROI} (\mathbf{R}_5[\lambda_c][i] - \mu_{R_5}[\lambda_c])^2 \right)^{\frac{1}{2}} \quad (29)$$

$\mu_{\sigma_{R_5}}[\lambda_c]$ (eq. 30) gives the average of the random noise of each pixel, and neglects the contributions of surface spatial nonuniformity and instrument fixed pattern noise.

$$\mu_{\sigma_{R_5}}[\lambda_c] = \frac{1}{20 \times 20} \sum_{i \in ROI} \sigma_{R_5}[\lambda_c][i] \quad (30)$$

We represent the pixel-level noise with the standard deviation of $\mathbf{R}_5[\lambda_c]$, $\sigma_{R_5}[\lambda_c]$ (eq. 31, with explicit λ_c dependence notation dropped for brevity), that we compute by propagating the standard deviations, $\sigma_{\Phi_5}[\lambda_c]$ and $\sigma_{\Phi_{99}}[\lambda_c]$, of the digital flux images $\Phi_5[\lambda_c]$ and $\Phi_{99}[\lambda_c]$, also accounting for the uncertainty on $R_{99}[\lambda_c]$, $\sigma_{R.99}[\lambda_c]$, that we compute as the unbiased weighted standard error on the mean (Bevington, 1969).

$$\sigma_{R_5} = \mathbf{R}_5 \left(\left(\frac{\sigma_{\Phi_5}}{\Phi_5} \right)^2 + \left(\frac{\sigma_{\Phi_{99}}}{\Phi_{99}} \right)^2 + \left(\frac{\sigma_{R.99}}{R_{99}} \right)^2 \right)^{\frac{1}{2}} \quad (31)$$

We compute σ_{Φ_5} and $\sigma_{\Phi_{99}}$ by propagating the standard deviation σ_{S_5} and standard error $SE_{S_{99}}$, of the images \mathbf{S}_5 and $\bar{\mathbf{S}}_{99}$ over the n_5 and n_{99} repeat observations, and the standard errors, SE_{D_5} and $SE_{D_{99}}$, of the associated dark images \mathbf{D}_5 and $\bar{\mathbf{D}}_{99}$ over the n_d repeat dark frames, and the standard error, SE_F , on the flat-field \mathbf{F} . Note that the standard deviation is used as the error on the single-frame image of \mathbf{S}_5 , whereas the standard error (on the mean) is used for the error on all other contributing images, under the assumption that the contributing factors will also have low noise contributions to the calibration of in-flight OROCHI images. We perform the propagation with equations 32 and 33.

$$\sigma_{\Phi_5} = \Phi_5 \left(\left(\frac{SE_F}{\mathbf{F}} \right)^2 + \frac{\sigma_{S_5}^2 + SE_{D_5}^2}{(\mathbf{S}_5 - \bar{\mathbf{D}}_5)^2} \right)^{\frac{1}{2}} \quad (32)$$

$$\sigma_{\Phi_{99}} = \Phi_{99} \left(\left(\frac{SE_F}{\mathbf{F}} \right)^2 + \frac{SE_{S_{99}}^2 + SE_{D_{99}}^2}{(\bar{\mathbf{S}}_{99} - \bar{\mathbf{D}}_{99})^2} \right)^{\frac{1}{2}}$$

(33)

We compute the error on the normalised reflectance by propagating the uncertainty on the reflectance, as

$$\sigma_{\varepsilon N}[\lambda_c] = N_{R_5}^{550}[\lambda_c] \left(\left(\frac{\varepsilon[\lambda_c]}{\mu_{R_5}[\lambda_c]} \right)^2 + \left(\frac{\varepsilon[550]}{\mu_{R_5}[550]} \right)^2 \right)^{\frac{1}{2}} \quad (34)$$

where ε is substituted for the given uncertainty.

From each of these metrics of uncertainty we compute and report an associated signal-to-noise ratio. We define:

$$SNR_s[\lambda_c] = \frac{\mu_{R_5}[\lambda_c]}{s_{R_5}[\lambda_c]} \quad (35)$$

$$SNR_{\mu_{\sigma}}[\lambda_c] = \frac{\mu_{R_5}[\lambda_c]}{\sigma_{R_5}[\lambda_c]} \quad (36)$$

and we also compute the pixel-wise SNR image, SNR_{R_5} , that we define as

$$SNR_{R_5}[\lambda_c] = \frac{\mathbf{R}_5[\lambda_c]}{\sigma_{R_5}[\lambda_c]} \quad (37)$$

In our analysis, we review these measures of signal-to-noise ratio, with consideration of factors such as the spatial nonuniformity of the sample, to draw conclusions on the ability of LOROS, and by proxy OROCHI, to fulfil the performance requirements of the MMX mission.

4 Results

Here we report the results of the characterisation experiments alongside the expected values for LOROS and OROCHI when downsampled to 12-bit digital output, denoted OROCHI¹², and, where appropriate, the off-the-shelf configuration of LOROS, denoted LOROS*.

4.1 Spatial Sampling

We observed a peak MTF_{Nyq.} of 0.43 ± 0.02 at 475 nm, and a consistent decrease toward longer wavelengths to 0.22 ± 0.01 at 950 nm, and a decrease toward shorter wavelengths to 0.31 ± 0.02 at 400 nm. The mean MTF_{Nyq.} values with $\pm 1\sigma$ errors are shown in comparison to the required values for OROCHI in figure 2, and given in table 1.

Table 1 Comparison of Spectral and Spatial Sampling of OROCHI¹² against expected and observed values for LOROS. Columns give the lens aperture (F/#), filter central wavelength (CWL) and full-width-at-half-maximum (FWHM), carbonaceous chondrite expected reflectance (R) computed with eq. 17, and Modulation Transfer Function at the sensor Nyquist frequency.

Band	F/#	CWL (nm)		FWHM (nm)		Expected $R(\lambda)$	MTF at Nyquist	
		OROCHI	LOROS	OROCHI	LOROS		OROCHI	LOROS
1	6.4	390	400	50	50	0.0317	0.2	0.31±0.02
2	6.4	480	475	30	25	0.0395	0.3	0.43±0.02
3	6.4	550	550	30	25	0.0424	0.3	0.39±0.02
4	6.4	650	650	40	50	0.0408	0.3	0.32±0.02
5	6.4	730	725	40	50	0.0395	0.3	0.29±0.03
6	6.2	860	850	40	50	0.0408	0.3	0.26±0.02
7	5.8	950	950	60	50	0.0408	0.2	0.22±0.01
8	6.4	550	550	30	25	0.0424	0.3	0.42±0.01

4.2 Sensor Response

Here we report the sensor characterisation results over the 4 experiments, F*S99L10, F*S5L10, FGS99L10 and FGS99L2.

4.2.1 Exposure vs Mean Signal

The relationship between exposure and mean signal for each camera and for each experiment is shown in figure 3. The linear regressions on the data are shown, illustrating the breakdown in linearity as $\mu_S \rightarrow S_{Max}$. Also shown are the expected digital flux values for OROCHI¹² at Phobos, that we have computed using the exposure times predicted by Kameda et al. (2021) for achieving SNR=120 in each band, via equation 38.

$$\Phi_{\text{OROCHI}^{12}\text{@Phobos}} = \frac{\text{SNR}^2}{n_{fw}} \frac{S_{Max}}{t_{exp}} \\ = \frac{120^2}{20000} \frac{4095}{t_{exp}} \quad (38)$$

Experiments F*S99L10 and F*S5L10 used a range of exposure values that can be considered typical for a reflectance experiment performed with LOROS, when imaging white Spectralon (SCT99) and a low reflectance target (e.g. SCT5). For images of SCT99, the exposure values of complete saturation (t_{max}) spanned the range 0.0023 s for Band 5 (725 nm) to 0.1058 s for Band 7 (950 nm), and for images of SCT5, the values spanned 0.0425 s, also for Band 5 (725 nm) to 1.6305 s, also for Band 7 (950 nm). The complete list of t_{max} values and fitted digital flux Φ for each experiment and band are given in table 2.

4.2.2 Photon and Dark Transfer Curves

The relationships between the temporal read and shot noise σ_{rs} and the mean signal μ_S for all cameras and illuminated experiments are illustrated by the photon-transfer curve, plotted in figure 4. The accompanying relationships under dark conditions are illustrated by the dark-transfer curve, plotted in figure 5. Also illustrated are the expected read noise, sensitivity and

saturation capacity values for OROCHI¹², LOROS and LOROS*. The values for σ_r and $\mu_{S,sat}$ observed for each band in comparison to those expected for OROCHI¹², LOROS* and LOROS are given in table 3 in columns 1 and 3, in units of DN. These values have been averaged over the results of the four experiments, except for $\mu_{S,sat}$, where the F*S5L10 experiment results were excluded from the average, as the lower spatial homogeneity of the SCT5 target has the effect of biasing the apparent saturation of the ROI. From the Dark Transfer Curve we observe a mean read noise of 0.97 DN, and from the Photon-Transfer Curve we observe a mean saturation capacity of 3899.39 DN, at 95% of the 12-bit sensor digital range, compared to expected LOROS values of 1.45 DN and 4041.44 DN, and expected OROCHI¹² values of 2.05 DN and 3988.32 DN, respectively.

4.2.3 Sensitivity

The values for K extracted from the photon-transfer curve as a function of μ_S are shown in figure 6, illustrating the spread of values about the expected values for OROCHI¹² and LOROS, in contrast to the expected value for LOROS*, prior to the gain adjustment. The expected shot-limited gradients of the photon-transfer curve are also illustrated in figure 4. The fitted values for each experiment and each channel are given in the histogram of figure 6, and the average results for each and across all bands are reported in row 6 of table 3. We observe a mean sensitivity of 4.75 e⁻/DN, compared to an expected LOROS value of 4.86 e⁻/DN, and an expected OROCHI¹² value of 4.88 e⁻/DN.

4.2.4 Linearity

The linearity errors for each camera, computed from regressions on the data illustrated in figure 3, over the range set by the $\mu_{S,sat}$ values derived from the photon-transfer curve, are shown in figure 7, with the fitted nonlinearity correction curves. The data is shown for experiments FGS99L2, FGS99L10 and F*S5L10. We found that the linearity error results for F*S99L10 exhibited a greater variance, that we attribute to the

Table 2 Measured digital flux and maximum exposure time for the various illumination conditions, in comparison to expected illumination of OROCHI¹² at Phobos. For each experiment digital flux was fitted to mean signal vs exposure data, measured over a 28×28 pixel uniformly illuminated area of the SCT99 (S99) and SCT5 (S5) Spectralon™ reference calibration target, using the designated filter for each channel (F*) and the same 550 nm filter for each channel (FG), and at arbitrary lamp brightness settings of 10 (L10) and 2 (L2).

Band	Φ DN/s					t_{max} s			
	F*S5L10	F*S99L10	FGS99L10	FGS99L2	ORO. ¹² @Ph.	F*S5L10	F*S99L10	FGS99L10	FGS99L2
1	4110.40	83709.0	70821.2	1566.27	29781.8	1.132285	0.051035	0.061241	2.753051
2	19143.8	387230.0	72729.0	1609.49	41526.8	0.263333	0.011869	0.058325	2.753051
3	64723.0	1279340	78481.5	1732.16	39843.2	0.073491	0.003975	0.055548	2.497099
4	33400.6	622920	89286.0	1975.72	34283.7	0.152392	0.006868	0.047984	2.157088
5	117274	2184080	63769.3	1410.87	21060.0	0.042529	0.002300	0.067519	3.035239
6	14093.6	241744	78159.8	1725.07	6017.1	0.316000	0.020510	0.055548	2.497099
7	2850.08	46638.4	76652.7	1696.65	3510.0	1.630491	0.105827	0.055548	2.621954
8	60831.0	1196380	90575.8	2004.86	39843.2	0.073491	0.003975	0.047984	2.157088

Table 3 Measured sensor properties of LOROS vs expected values for OROCHI¹², LOROS and LOROS*. Sensor properties measured by photon transfer and dark transfer experiments for each band of LOROS (1–8), and averaged across these bands (Ave.), with the expected properties of the sensors of OROCHI (equivalent if downsampled to 12-bit output), LOROS* (pre-configuration) and LOROS (post-configuration) derived from datasheets (OnSemi., 2015; Sony Corporation, 2015).

Metric	Expected			Ave.	Band Measurements							
	ORO. ¹²	LOROS*	LOROS		1	2	3	4	5	6	7	8
σ_r (DN)	2.05	0.89	1.45	0.97	0.95	0.98	0.99	1.05	0.98	1.02	0.76	1.06
σ_r (e ⁻)	10.00	7.07	7.07	4.62	4.46	4.68	4.70	4.98	4.70	4.84	3.59	5.02
$\mu_{S.sat}$ (DN)	3988	4041	4041	3899	3835	3809	3880	3932	3961	3962	3913	3902
$\mu_{e.sat}$ (e ⁻)	19474	32247	19656	18503	17979	18332	18558	18557	19000	18722	18398	18478
n_{FW} (e ⁻)	20000	32682	19921	19441	19236	19628	19511	19442	19629	19393	19238	19449
K (e ⁻ /DN)	4.88	7.98	4.86	4.75	4.70	4.79	4.76	4.75	4.79	4.73	4.70	4.75
LE (%)	1.00	0.37	0.37	0.43	0.34	0.35	0.39	0.38	0.79	0.38	0.41	0.40
Φ_d (DN/s)	0.53	1.10	1.81	1.35	1.48	1.15	1.45	1.32	1.31	1.03	1.78	1.27
Φ_d (e ⁻ /s)	2.60	8.80	8.80	6.40	6.96	5.51	6.91	6.24	6.27	4.89	8.35	6.04
SNR _{Max}	140	180	140	135	134	135	135	136	137	136	135	135
DR (bits)	10.97	12.17	11.46	12.04	12.08	12.03	12.02	11.93	12.03	11.97	12.39	11.92
Bias (DN)	NA	NA	4.00	5.07	5.00	5.12	5.21	5.09	5.18	5.32	4.49	5.13
PRNU (%)	0.90	0.45	0.45	0.40	0.37	0.34	0.35	0.53	0.42	0.38	0.34	0.45
DSNU (DN)	10.50	0.11	0.18	0.24	0.22	0.23	0.24	0.28	0.26	0.25	0.18	0.26

Table 4 Polynomial nonlinearity correction model coefficients for each band, fitted to linearity error data from experiments FGS99L2, FGS99L10 and F*S5L10.

Band	nl_0	nl_1	nl_2
1	-1.811E-01	4.1820E-04	-1.6992E-07
2	-1.9136E-01	5.7728E-04	-1.9488E-07
3	-1.4765E-01	4.7686E-04	-1.7225E-07
4	-1.9191E-01	6.2960E-04	-2.0741E-07
5	-1.5997E-01	5.0248E-04	-1.7596E-07
6	-1.1953E-01	4.4276E-04	-1.7572E-07
7	-7.7658E-02	3.1653E-04	-1.5060E-07
8	-1.1146E-01	3.8910E-04	-1.5642E-07

lower sampling density and thus greater weighting to low-signal/high-noise values, and have consequently excluded the results of F*S99L10 from the linearity evaluation. The average results for each and across all bands are reported in row 7 of table 3. We observe a mean linearity error of 0.43%, compared to an expected LOROS value of 0.37%, and an expected OROCHI¹² value of 1%. We observe that typically the linearity error crosses 0% in the region of 2000–2500 DN. The nonlinearity correction model coefficients fitted to the linearity error data are given in table 4.

4.2.5 Saturation Capacity

Using the values for K obtained for each channel we converted $\mu_{S.sat}$ DN to $\mu_{e.sat}$ e⁻, with the resultant values given in row 4 of table 3. We observe a mean saturation capacity of 18503 e⁻, compared to an expected LOROS value of 19656 e⁻, and an expected OROCHI¹² value of 19747 e⁻. We observe a mean effective full-well of 19441 e⁻, compared to an expected LOROS value of 19921 e⁻, and an expected OROCHI¹² value of 20000 e⁻.

4.2.6 Read Noise, Bias & Dark Current

The bias and dark current of each band are illustrated in figure 8, that shows the dark-transfer data in comparison to the expected dark signal, according to the programmed bias (of 4 DN). Using the values for K obtained for each channel we converted σ_r DN to σ_r e⁻, with the resultant values given in row 2 of table 3. We observe a mean read noise of 4.62 e⁻, compared to an expected LOROS value of 7.07 e⁻, and an expected OROCHI¹² value of 10.00 e⁻. From the dark-transfer data we computed values for the dark current of each band, that are reported in units of DN/s and converted to e⁻/s (via K) in rows 11 and 12 of table

3. We observe a mean bias of 5.07 DN, compared to a programmed bias of 4 DN. We observe a mean dark current of $6.40 \text{ e}^-/\text{s}$ (1.35 DN/s), compared to an expected LOROS value of $8.80 \text{ e}^-/\text{s}$ (1.81 DN/s), and an expected OROCHI¹² value of $2.60 \text{ e}^-/\text{s}$ (0.53 DN/s).

4.2.7 SNR & Dynamic Range

From the values of $\mu_{e.\text{sat}}$ we computed SNR_{Max} for each band, reported in row 13 of table 3. We observe a mean SNR_{Max} of 135.30, compared to an expected LOROS value of 140.2, and an expected OROCHI¹² value of 139.55. From the values of $\mu_{e.\text{sat}}$ and σ_r we computed the dynamic range, in units of dB and bits. We observe a mean DR of 72.00 dB (12.04 bits), compared to an expected LOROS value of 11.46 dB (11.46 bits), and an expected OROCHI¹² value of 66.02 dB (10.97 bits). In figure 9 we have plotted the SNR for each data-point of the photon-transfer curve, computed as $\text{SNR} = \mu_S / \sigma_{rs}$, to illustrate the range of μ_S for which the minimum SNR requirement of 100 is satisfied, and to illustrate the variance of the derived values.

4.2.8 PRNU & DSNU

We evaluated the PRNU over the ROI used for the photon-transfer data in each band, from the mean flat-field images that were recorded for each band and each wavelength. We observe a mean PRNU of 0.40%, compared to an expected LOROS value of 0.45%, and an expected OROCHI¹² value of 0.90%. We evaluated the DSNU by averaging the standard deviation of dark frames over the ROI used for the photon-transfer experiments in the short-exposure regime of $t_{\text{exp}} < 10 \text{ ms}$. We observe a mean DSNU of 0.24 DN, compared to an expected LOROS value of 0.18 DN and an expected OROCHI¹² value of 10.5 DN. However, we note that the value provided for OROCHI is derived from the quoted maximum tolerance, as opposed to the nominal value, so we expect the sensors used for the OROCHI Flight Model to exhibit lower DSNU values.

4.3 Reflectance Simulations

The results of the simulated reflectance sampling of the example carbonaceous chondrite reflectance spectra are illustrated in figure 10. The numerical values of the sampled reflectance are given in table 1, with the CWL and FWHM values of OROCHI and LOROS. The shaded transmission profiles of figure 10 illustrate the spectral sampling differences between LOROS and OROCHI, and the positions of the data points illustrate the implications of these differences on the observed data. We see that the maximum change in CWL is 2.6% for Band 1, and the maximum change in FWHM is 25%, for bands 4, 5 and 6. We see that

these changes in CWL and FWHM manifest as a maximum change in observed reflectance of the carbonaceous chondrite of +3.0% in Band 1, -0.9% in Band 2, with all other bands changing by $\leq 0.1\%$.

We observe simulated mean and standard deviation values of the $\sim 0.7 \mu\text{m}$ absorption feature as 0.0465 ± 0.0114 for LOROS and 0.0463 ± 0.0116 for OROCHI, with associated SNR values of 4.09 and 3.99 respectively.

4.4 Reflectance Measurements

The subframes showing the images captured of SCT5 in each band are shown in figure 11, illustrating the similarity in image histograms over the selected illuminated area of the ROIs, achieved through exposure times (t_5) found by the auto-exposure routine, given in table 5. The t_5 minimum and maximum values were 0.07 s for Band 5 (725 nm) and 3.21 s for Band 7 (950 nm), in comparison to exposure values for SCT99 (t_{99}), also reported in table 5, of 0.004 s for Band 5 and 0.195 for Band 7. Figure 12 shows the recovered reflectance factor for each pixel across the ROI for each Band, illustrating the spatial heterogeneity of the SCT5 sample, and the similarity of the spatial pattern for each ROI. We report the average reflectance across each ROI (μ_{R_5}) for each Band, with the evaluated ROI spatial and mean temporal noise, and the associated SNR values, in table 5, in columns 6, 7, 8, 13 and 14 respectively, with the resampled reference reflectance for SCT5 given in column 5. We observe reflectance values of 4.51 (400 nm)–5.81 % (950 nm), in comparison to reference values of 4.70 (400 nm)–6.15 % (950 nm) with temporal noise values of 0.004–0.005 %, and associated temporal SNR values of 121.6–124.3. We observe spatial standard deviations of 0.12–0.17 %, corresponding to spatial-limited SNR values of 40.7–28.3. We report the reference and observed normalised reflectance factors in columns 9 and 10, with observed values of 0.944 (400 nm)–1.215 (950 nm) in comparison to reference values of 0.942 (400 nm)–1.234 (950 nm).

Figure 13 shows the spatial distribution of the pixel-wise temporal SNR across the ROI of each Band, with the histogram of each channel showing a peak of ~ 120 SNR, and that the majority of pixels have $\text{SNR} > 100$. The normalised reflectance factor (against the 550 nm channel) is plotted against the normalised reference reflectance factor in figure 14. The error bars represent the spatial nonuniformity ($\sigma_{s.N}$) and the temporal noise ($\sigma_{\mu_{\sigma}.N}$) of the observed values, given in columns 11 and 12 of table 5. Figure 15 shows the SNR as a function of wavelength, illustrating the difference between the values for SNR_S and $\text{SNR}_{\mu_{\sigma}}$.

Table 5 Results of the SCT5 reflectance factor measurement experiment. For each band of LOROS (1–8), columns give the exposure times used for imaging of SCT99 (t_{99} s) and SCT5 (t_5 s), the expected reflectance factor (R_5), the mean reflectance factor observed over the ROI (μ_{R_5}), the spatial and temporal noise over the ROI (s_{R_5} , $\mu_{\sigma_{R_5}}$), the Band-3 (550 nm) normalised expected reflectance factor and mean reflectance factor ($N_{R_5}^{550}$, $N_{\mu_{R_5}}^{550}$) and associated spatial and temporal noise ($\sigma_{s.N}$, $\sigma_{\mu_{\sigma}.N}$), and the spatial and temporal Signal-to-Noise Ratios (SNR_s, SNR _{μ_{σ}}).

Band	CWL (nm)	t_5 (s)	t_{99} (s)	$R_5 \times 10^{-2}$	$\mu_{R_5} \times 10^{-2}$	$s_{R_5} \times 10^{-2}$	$\mu_{\sigma_{R_5}} \times 10^{-2}$	$N_{R_5}^{550}$	$N_{\mu_{R_5}}^{550}$	$\sigma_{s.N}$	$\sigma_{\mu_{\sigma}.N}$	SNR _s	SNR _{μ_{σ}}
1	400	1.4297	0.0676	4.697	4.514	0.016	0.0037	0.942	0.944	0.040	0.011	29.1	121.6
2	475	0.3195	0.0157	4.817	4.674	0.016	0.0038	0.966	0.977	0.040	0.011	29.8	122.3
3	550	0.1138	0.0056	4.985	4.783	0.012	0.0039	1.000	1.000	0.035	0.011	40.7	123.4
4	650	0.2064	0.0109	5.239	5.022	0.015	0.0041	1.051	1.050	0.041	0.012	33.0	122.9
5	725	0.0709	0.0038	5.444	5.185	0.015	0.0042	1.092	1.084	0.041	0.012	34.2	123.3
6	850	0.4668	0.0271	5.821	5.573	0.015	0.0045	1.168	1.165	0.043	0.013	36.0	124.3
7	950	3.2055	0.1946	6.151	5.810	0.016	0.0047	1.234	1.215	0.045	0.014	36.6	123.6
8	550	0.0991	0.0050	4.985	4.787	0.017	0.0039	1.000	1.001	0.043	0.011	28.3	122.9

5 Discussion

In this section we discuss the differences and similarities between the observed and expected LOROS characteristics, and those expected for OROCHI¹², and the implications of these on future imaging experiments with LOROS, and on OROCHI in-flight operations.

5.1 Spatial Sampling

Our observed values of the LOROS MTF exceed the OROCHI requirement values over the 400–550 nm range by $\gtrsim 30\%$, and agree within $\pm 15\%$ over the 650–950 nm range. As the final MTF values of the Flight Model of OROCHI are currently unknown, the observed similarities of LOROS MTF values over the OROCHI requirement values demonstrate that LOROS is a suitable representation of the expected optimal spatial sampling of OROCHI. Strictly, to replicate the expected imaging conditions of OROCHI from the landed configuration of the MMX spacecraft, we should degrade the image quality in all but Band 8, by either defocusing of the lenses or by Gaussian blurring with a kernel of radius determined by the expected MTF. For the purposes of this study, we wish to demonstrate the ability of LOROS to globally map the 0.7 μm absorption feature; this demonstration requires spatially resolved pixels, hence we have performed the experiments with optimal focus for the 0.8 m object distance. As it is simple to degrade an image by Gaussian blurring, we recommend that future experiments are also performed with all channels optimally focused, and that investigations of the ability to recover reflectance from de-focussed images be performed on digitally blurred images, requiring knowledge of the expected MTF for each band at the 0.8 m working distance. For this reason we recommend an investigation of the expected OROCHI MTF of each band at the 0.8 m working distance.

5.2 Sensor Response

Here we discuss the observed and expected characteristics of the response of the LOROS sensor (IMX249) in contrast to the expected response of the OROCHI sensor (KAI-08051).

5.2.1 Exposure vs Mean

The relationship between signal and exposure time, shown in figure 3, illustrates the range of sensor illumination conditions (intensity and wavelength) represented by the 4 experiment configurations, showing that we have characterised the 8 cameras of LOROS over ranges of $t_{exp} \lesssim 50$ ms (short-exposure regime) through to $t_{exp} \lesssim 3$ s (long exposure regime). Although reproduction of the illumination conditions at Phobos was not a strict requirement of this experiment, we find that images of SCT5 under the brightest lamp setting (10) produce a digital flux in each channel that is comparable to the digital flux for OROCHI¹² at Phobos, as visualised in the top right plot of figure 3. This figure also shows that the digital fluxes for Bands 1 and 7 (400 nm and 950 nm) are distinctly lower than 2–6 (475 nm–850 nm), an expected consequence of the low silicon quantum efficiency and low illumination in these regions of the spectrum. For the FG experiments (all Bands imaged using the 550 nm filter) we note that the digital flux values are not identical, implying a difference in response between the cameras. The SCT99 target is approximately isotropic; under this assumption we expect the radiance on the lens for each camera to be approximately equal, implying that the dominant differences are intrinsic to the cameras. As figures 4 and 6 imply approximately equal sensitivity of all LOROS camera sensors, we suggest that the dominant differences are due to the use of the F/16 aperture stop, where the aperture diameter is very small, and may approach the scale of manufacturer tolerance in the mechanical design of the adjustable aperture. For

the experiments with the apertures set to F/5.8–6.4 we do not expect such deviation of the aperture diameter from the expected value, due to the larger aperture diameters, and due to the method used for tuning the apertures, with respect to the F/1.4 position, that inherently corrects for any mechanical differences in the aperture mechanism, under the assumption that the F/1.4 aperture diameter is large relative to the mechanical tolerance.

5.2.2 Photon- and Dark- Transfer Curves

The Photon Transfer Curve (fig. 4) shows that the noise characteristics of the sensors of each band of LOROS have similar performance to one another, that is independent of the spectral sampling and irradiance domain, that were varied across experiments F*S99L10, F*S5L10, FGS99L10 and FGS99L2. We see from figure 4 that the adjustment of the gain to 4.30 dB has succeeded in bringing the $\sqrt{\mu_S/K}$ noise response (top) and $\mu_{e,sat}$ saturation capacity (bottom) of LOROS close to that expected of OROCHI¹². By comparison of the trend of (μ_e, σ_{rs}) data points to the shot-noise slope in the electron domain (fig. 4 bottom), we see that for exposures that accumulate $\gtrsim 10^3$ e⁻ (i.e. $\gtrsim 5\%$ of the pixel capacity) the sensors operate in the shot-limited noise regime. The observed read noise of LOROS shown in the dark transfer curve (fig. 5) is lower than expected (Band average of 0.98 DN vs. 1.45 DN) under the 4.3 dB gain configuration, and closer to the expected read noise for the 0.0 dB gain configuration (0.89 DN). This implies that the dominant contributions to the read noise occur after amplification, e.g. during analog-to-digital conversion, such that increasing the gain has not effected the observed read noise, and thus we expect to maintain a high dynamic range with LOROS.

5.2.3 Sensitivity

As observed from the photon-transfer curve, we can also see from figure 6 that the application of the 4.3 dB gain has produced observed $(\mu_S[k], K[k])$ trends in each band with mean K values that are close to that expected of OROCHI¹². The band-averaged observed sensitivity of LOROS is 2.7% lower than the expected sensitivity of OROCHI¹², such that for a given shot-limited signal, the associated SNR for LOROS will be 1.3% lower than for OROCHI¹². The implication is that to achieve a given SNR requires a 2.7% increase in exposure of LOROS in comparison to OROCHI¹²; e.g. an SNR of 100 would be expected for a signal of 2049 DN for OROCHI¹², and 2105 DN for LOROS. It is simple to correct for this difference by increasing the image exposure, but at the expense of dynamic range; i.e. the number of DN values available that achieve

>100 SNR. As LOROS is a laboratory simulator, we expect the scenes that we image to have a low dynamic range relative to the scenes that OROCHI will encounter in-flight at Phobos, and so we do not anticipate this small reduction in dynamic range to cause issue.

5.2.4 Linearity

The measurement of the linearity error has confirmed that the use of a CMOS architecture sensor has not introduced a significant nonlinearity to the system, in comparison to that expected of the CCD sensor architecture for OROCHI. Indeed, we have confirmed a lower mean linearity error of 0.43% compared to an expectation of 1% for OROCHI. The demonstration of reproducible $(\mu_S[k], \varepsilon[k])$ curves in each band for the range of digital fluxes of experiments FGS99L2, FGS99L10 and F*S5L10 confirms that the fitted nonlinearity correction curves can be applied to LOROS images over the short and long exposure regimes as a function of the signal (S DN).

5.2.5 Saturation Capacity

As evidenced in figure 4 (bottom), the 4.3 dB gain adjustment has successfully brought the saturation capacity of LOROS inline with the expectation of OROCHI (note that in the electron domain there is no distinction between OROCHI and OROCHI¹²). We observe a band-averaged saturation capacity ($\mu_{S,sat}$ DN) that is 3.5% lower than the expected (PRNU corrected) saturation capacity for LOROS. Given that we also observe a PRNU value that is 11% lower than expected, this implies that the spatial nonuniformity of the illumination pattern across the ROI was the dominant source of fixed-pattern noise in our experimental setup. We can use the effective full-well capacities (eq. 8) observed and expected for LOROS, OROCHI¹² and LOROS* to correct for the effects of the illumination nonuniformity. The observed effective full-well for LOROS is 2.4% lower than expected, a consequence of the estimate of n_{FW} being derived from K (eq. 9), with an implication of a reduced >100 SNR dynamic range, as discussed previously in the context of K .

5.2.6 Read Noise, Bias & Dark Current

We have already noted the lower than expected read noise for LOROS in the digital signal domain; we also note that the read noise is lower than expected in the electron domain, which serves to increase the dynamic range of the sensor. However, as our primary concern is achieving pixel-level SNR of >100 , and as we have noted the sensor operates under shot-limited conditions for pixel exposures $>5\%$ of the sensor range, the small change in read noise is not of concern to

our study. The small (~ 1 DN) discrepancy between the programmed bias (4 DN) and the observed bias (5.07 DN) does not significantly affect the dynamic range of the sensor, in comparison to the 2.5% discrepancy in effective full-well. Although the observed band-averaged dark current is lower than expected for LOROS (-27%), this is larger than the expected OROCHI dark current by a factor of ~ 3 . However, for the expected operational exposures of OROCHI at Phobos, and for experiments with LOROS, we do not expect this discrepancy to have significant implications on the temporal noise of LOROS images, for the following reasons. From the dark-transfer curve (fig. 5 top) we can see that noise associated with the dark signal becomes shot dominated for $\mu_D \approx 50$ DN, that we see via figure 8 occurs for $t_{exp} \gtrsim 20$ s. This implies that the $3\times$ difference in dark current between LOROS and OROCHI will only begin to degrade the SNR in observably different ways for exposures exceeding 20 s. This provides sufficient contingency for imaging experiments of materials with reflectance down to $\sim 1\%$, where we may expect a 5-fold increase in the exposure (e.g. bringing the expected 950 nm exposure from 3.2 s to ~ 16 s).

5.2.7 SNR & Dynamic Range

The (μ_S, SNR) relationship illustrated in figure 9 clearly demonstrates the close agreement in the performance between the observed SNR of each LOROS band and that expected of LOROS and OROCHI¹². This visualisation shows the SNR crosses 100 for $\mu_S > 2100$ DN, such that approximately 50% of the sensor response range produces a signal with >100 SNR. This demonstrates that images exposed with LOROS and OROCHI¹² of identical scenes with identical exposures will produce images with similar signal-to-noise ratios (with a $\sim 1.3\%$ difference). The spread of $\text{SNR}[k]$ values about the mean lines indicate that the SNR computation is sensitive to noise, and provides context to the difference between the observed and expected SNR trend lines and the tolerance of the SNR observations. In table 3 we presented the SNR_{Max} performance metric as defined by the EMVA 1288, from $\mu_{e,sat}$, that we computed with estimates of the effects of the PRNU on the expected values for OROCHI¹² and LOROS, yielding an observed band-averaged SNR_{Max} 3% below that expected of OROCHI¹². As discussed, we interpret our measure of $\mu_{e,sat}$ to be underestimated due to the pattern illumination dominated fixed-pattern noise. Computing the SNR_{Max} from the estimated effective full-well yields SNR_{Max} values for OROCHI¹², LOROS*, LOROS, and the band-averaged LOROS observations of: 141.42, 180.78, 141.14 and 139.43 respectively. Under this interpretation of SNR_{Max} we see a closer agreement between OROCHI¹² and band-averaged LOROS

observations, of -1.4%. The observed dynamic range for LOROS is 5% greater than expected, and 10% greater than expected for OROCHI. However, as discussed, the upper limit ($\mu_{e,sat}$) defining the dynamic range for LOROS is lower than OROCHI, whilst the lower limit (σ_r) is lower, thus we attribute the extended dynamic range to the low read noise. As our primary concern is the noise response in the upper half of the sensor range, we do not consider this extended dynamic range of LOROS over OROCHI to indicate a significant difference in performance. If, however, future experiments include the analysis of shaded regions of a scene, then this difference in the low-signal regime noise response should be considered.

5.2.8 PRNU & DSNU

As discussed previously, the observed PRNU for LOROS is lower than that of OROCHI. In the context of the $\sim 2\%$ nonuniformity across the pattern illumination, we see that indeed the pattern illumination dominates the fixed-pattern noise of the experiment over the PRNU 0.4% contribution. The observed 0.24 DN DSNU is significantly lower than the expected 10.5 DN of OROCHI¹², but we note that the OROCHI value is an upper tolerance limit, rather than an expected value (OnSemi., 2015). The low ($<< 1$ DN) DSNU has the implication that we can expect to produce a good approximation of the true signal with a bias correction only. That is, under experimental circumstances where dark frame capture is not practical or is subject to some corrupting error, the observed bias values for each channel (table 2) can be used in substitute of the complete dark frame correction (of eqs. 24, 25).

5.3 Reflectance Simulations

Our simulated analysis of spectral sampling of the candidate carbonaceous chondrite reflectance spectrum with the OROCHI and LOROS filter sets shows that the small ($\lesssim \pm 3\%$) change in CWL and moderate ($\lesssim \pm 25\%$) change in FWHM result in changes below the noise equivalent (for $\text{SNR}=100$) in all but Band 1 (390 nm), where a change in reflectance of 3% is predicted. In the 500 nm–1000 nm range the change in Band 5, which approximately samples the centre of the 0.7 μm hydration feature, results in an expected change in observed reflectance of $\lesssim 0.1\%$, that would not significantly affect the measurement of band-depth for an observation with an SNR of 100. For the gradients of these samples in the 600–700 nm region, the change in FWHM for Band 5 (650 nm) has a negligible effect on the sample reflectance. The change in CWL of the 390, 480, 730 and 860 nm channels results in a change in sampled reflectance that is perceptible at the scale of the figure, but these changes are typically within the error bounds ($\pm 1\sigma$). Crucially, the

simulated band-depth measurement results show that both OROCHI and LOROS can be expected to resolve the $\sim 0.7 \mu\text{m}$ hydration-correlated absorption feature to 4σ , from reflectance measurements in each channel with SNR=100.

5.4 Reflectance Measurements

The distribution of pixel values for each band illustrated in figure 11 shows that our auto-exposure routine and settings are capable of reliably exposing images to equivalent levels, such that all pixels within the ROI have $\text{SNR} > 100$ ($S > 2100 \text{ DN}$) and are not saturated. The colour bar for each band subplot indicates the change in mean value between the bands, in the range of ~ 3000 – 3100 DN , which notably is in the region of the steepest slope of the linearity error (fig. 7); nonlinearity introduced across the variance of pixel values within the ROI were corrected for as part of the pre-processing. In the context of the dark signal, for the longest exposure of 3.21 s (Band 7) we do not expect a significant change in the noise characteristics of the observation, as we expect the change in dark signal to be $< 1 \text{ DN}$ (fig. 8). We see that values for $t_{99}[\lambda_c]$ are, as expected, typically related to $t_5[\lambda_c]$ by a factor of $R_5[\lambda_c]/R_{99}[\lambda_c]$.

The observed reflectance factor of each band is consistently less than the expected reflectance factor, by ~ 0.002 , or -4.5% . If this discrepancy is intrinsic to the instrument, then the cause is either an overestimate of Φ_{99} or an underestimate of Φ_5 . The consistency of the offset across all channels implies that the error is not random, and is not related to the different exposure regimes used for the SCT99 and SCT5 image captures, that, across the bands, span the short and long exposure regimes (0.0038–0.194 s, 0.07–3.2 s respectively). Instead, we attribute the difference to be intrinsic to SCT5, SCT99, or both, implying that the directional-directional reflectance factor observed for SCT5 from each band position is consistently lower than the reference $8^\circ/\text{H}$ directional-hemispherical reflectance, or that that observed for SCT99 is consistently higher than the reference. This implies that the bidirectional-reflectance distribution function (BRDF) for SCT5, SCT99, or both, deviates from isotropic behaviour. Indeed, Shaw et al. (2016) demonstrate that for a fixed non-normal incidence illumination, the reflectance factor of SCT5 first decreases in reflectance factor for emergence angles up to $\sim 30^\circ$ – 40° , by up to $\sim 10\%$, before increasing, whilst SCT99 does not exhibit this decrease in reflectance factor, but remains approximately constant, before increasing after a similar range of emergence. With the LOROS configuration, recall our incidence angle is fixed at 30° , and the emergence values are 10.025° for the corner sites,

and 7.125° for all other sites. We hypothesize that the SCT5 BRDF is the dominant source of anisotropy. To test this hypothesised dependence of the SCT5 reflectance factor on the observation and illumination geometry, in future studies we must characterise the BRDF of the SCT5 sample, and indeed also the SCT99 sample used for the calibration, over the range of observation geometries used in the experiment.

We see that after conversion to reflectance factor we maintain SNR values of > 100 for most pixels in the ROI (fig. 13). Recall that we estimate the SNR from RMSE values over the $n_s = 25$ repeat frames; that is, a sample size much smaller than the 20×20 ROI (i.e. 400 samples) used for each point of the SNR plot of figure 9, hence the variance of SNR values and apparent loss of spatial correlation between the SNR images (fig. 12) against the signal images (fig. 11). When averaged over the ROI, we have achieved SNR values > 120 in all bands of LOROS, demonstrating fulfilment of the objective. In conjunction with the simulations of sampling of the $0.7 \mu\text{m}$ absorption feature, this demonstration implies that we can expect to observe the absorption feature, correlated with hydration, with $> 4\sigma$ accuracy.

Despite the expectation of SCT5 to approximate a spatially homogenous reflector, we see that the spatial variance of the signal dominates over the random noise. This is illustrated by the error bars displayed in figure 14, and in figure 15, where we see that the spatial variance has an associated SNR of ~ 30 – 40 , or $\sim \times 3$ – 4 lower than the temporal SNR. This demonstrates that over a 20×20 ROI the spatial variance of the reflectance factor of an approximately homogeneous material dominates over the instrument noise. We note that we can expect the natural scenes observed at Phobos to exhibit greater spatial variance than the SCT5 sample. For this reason, we recommend the calculation of spectral parameters (such as the band depth of eq. 20) to be performed for co-registered images at the pixel scale, rather than from statistical summaries of each band. This requires geometric calibration and correction of LOROS images, that we have not discussed in this paper.

The close agreement between the observed and expected normalised reflectance factors for LOROS (fig. 14) demonstrates the stability of performing the reflectance factor measurements across the 8 spectral channels from the 8 separate camera systems. This shows that the relative trends between the bands can be captured reliably, from which characteristics of the spectral profiles (e.g. eq. 20) can be computed.

6 Conclusion

We have described the configuration and characterisation of the Laboratory OROCHI Simulator, a mul-

tiview multispectral imaging system for performing extensive analogue imaging campaigns in preparation for operation of the MMX OROCHI imaging experiment at the martian moons, Phobos and Deimos. We performed simple computational simulations of the spectral sampling of LOROS in comparison to OROCHI, and demonstrated that the required minimum signal-to-noise ratio for reflectance factor measurements of 100 yielded an expected 4σ measurement of the $0.7 \mu\text{m}$ hydration-correlated absorption feature, that OROCHI will seek to map across the Phobos surface. We tuned the gain and offset of the COTS cameras used to simulate the bespoke OROCHI cameras to match the expected performance of the Flight Model, and by performing a series of Photon Transfer experiments at multiple illumination regimes and wavelengths we demonstrated empirical agreement of LOROS with the expected performance of OROCHI (in equivalent 12-bit signal quantisation) within $\sim 3\%$ for key metrics including sensitivity, effective full-well capacity and read noise. We established shot-limited behaviour of the sensors for exposures greater than 5% of the sensor range, and derived signal-to-noise ratio curves for each Band, showing that exposures of $>51\%$ of the sensor range achieve an expected SNR of >100 . We performed a reflectance factor measurement experiment on 5% reflectance grey SpectralonTM, by calibrating against observations of 99% reflectance SpectralonTM and demonstrated a mean temporal signal-to-noise ratio of 120 across all channels. We observed a -4.5% systematic offset across all channels, that we attribute to a hypothesized anisotropic bidirectional reflectance distribution function of the 5% SpectralonTM, that highlights the need to consider photometric effects when measuring near-field ($<1 \text{ m}$) reflectance factor with multiview spectral imaging systems. The configuration and characterisation of LOROS described here provides the foundation for continued preparatory investigations, including imaging of carbonaceous chondrites, and samples of asteroids Ryugu and Bennu, hosted at the ISO 6 JAXA ESCuC, and ultimately the imaging of the samples of Phobos that the MMX mission will return.

Abbreviations

ADC: Analog-to-Digital Convertor; BRDF: Bidirectional-Reflectance Distribution Function; CCD: Charge-Coupled Device; CMOS: Complementary Metal-Oxide-Semiconductor; COTS: Commercial Off-the-Shelf; CWL: Central Wavelength; DN: Digital Number; DR: Dynamic Range; DSNU: Dark Signal Non-Uniformity; EMVA: European Machine Vision Association; ESCuC: Extraterrestrial Sample Curation Centre; FoV: Field-of-View; fps: Frames per Second; FWHM: Full-Width-at-Half-Maximum; JAXA: Japan Aerospace Exploration Agency; LE: Linearity Error; LOROS: Laboratory OROCHI Simulator; MMX: Martian Moons eXploration; MP: Megapixel; MTF: Modulation Transfer Function; OD: Optical Depth; ONC-T: Optical Navigation Camera Telescope; OROCHI: Optical Radiometer composed of CHromatic Imagers;

PRNU: Photo-Response Non-Uniformity; QE: Quantum Efficiency; QSO: Quasi-Satellite Orbit; RMSE: Root-Mean-Square-Error; ROI: Region-of-Interest; SCT5: Spectralon Calibration Target 5%-reflectance; SCT99: Spectralon Calibration Target 99%-reflectance; SE: Standard Error; SNR: Signal-to-Noise Ratio; VNIR: Visible-to-Near-Infrared.

Availability of data and material

The datasets generated and/or analysed during the current study are available in the Zenodo repository, <https://doi.org/10.5281/zenodo.14028648>.

Competing interests

The authors declare that they have no competing interests.

Funding

RS and SK are supported by a Japan Society for the Promotion of Science Postdoctoral International Fellowship for Research in Japan (Short-term) PE22759.

Authors' contributions

RS: Conceptualisation, Methodology, Software, Validation, Formal Analysis, Investigation, Data Curation, Writing - Original Draft, Visualisation, Funding Acquisition; **SK:** Conceptualisation, Methodology, Resources, Writing - Review & Editing, Supervision, Project Administration, Funding Acquisition.

Authors' information

RS conducted this research as an JSPS International Research Fellow (College of Science, Rikkyo University), and is now at the Natural History Museum, London, UK. SK is the Principal Investigator for the OROCHI experiment of the JAXA MMX mission.

Acknowledgements

Not applicable.

Endnotes

¹Effective dynamic range defined here as $\log_2(e.\text{sat}/\sigma_r)$

²The orientation angle appears differently in each channel due to the separation on the optical bench.

³A standard calibration observation geometry, where illumination is from a narrow beam at 8° incidence to the target surface, and the reflectance is derived from the irradiance observed over the entire hemisphere (via integrating sphere).

References

- Allender, E.J., Cousins, C.R., Gunn, M.D., Caudill, C.M. (2020) Multiscale and Multispectral Characterization of Mineralogy with the ExoMars 2022 Rover Remote Sensing Payload. *Earth and Space Science* 7(4), 2019-000692. doi:10.1029/2019EA000692
- Barucci, M.A., Reess, J.-M., Bernardi, P., Doressoundiram, A., Fornasier, S., Le Du, M., Iwata, T., Nakagawa, H., Nakamura, T., André, Y., Aoki, S., Arai, T., Baldit, E., Beck, P., Buey, J.-T., Canalias, E., Castelnau, M., Charnoz, S., Chaussidon, M., Chapron, F., Ciarletti, V., Delbo, M., Dubois, B., Gauffre, S., Gautier, T., Genda, H., Hassen-Khodja, R., Hervet, G., Hyodo, R., Imbert, C., Imamura, T., Jordá, L., Kameda, S., Kouach, D., Kouryama, T., Kuroda, T., Kurokawa, H., Lapaw, L., Lasue, J., Le Deit, L., Ledot, A., Leyrat, C., Le Ruyet, B., Matsuoka, M., Merlin, F., Miyamoto, H., Moynier, F., Nguyen Tuong, N., Ogohara, K., Osawa, T., Parisot, J., Pistre, L., Quertier, B., Raymond, S.N., Rocard, F., Sakano, T., Sato, T.M., Sawyer, E., Tache, F., Trémolières, S., Tsuchiya, F., Vernazza, P., Zeganadin, D. (2021) MIRS: an imaging spectrometer for the MMX mission. *Earth, Planets and Space* 73(1), 211. doi:10.1186/s40623-021-01423-2
- Baumer Optronic GmbH. VCXG-24M EMVA 1288 Summary Sheet. Datasheet SN 700001878217, Technical and Application Support Center, Baumer Optronic GmbH (February 2017). SN 700001878217. https://www.baumer.com/medias/_secure_/_EMVA_VCXG-24M_CID010002_External.pdf?mediaPK=9021140598814
- Bevington, P.R. (1969) *Data Reduction and Error Analysis for the Physical Sciences*. McGraw-Hill, New York
- Bi, S., Gu, Y., Zhang, Z., Liu, H., Zhai, C., Gong, M. (2020) Multi-camera stereo vision based on weights. In: 2020 IEEE International Instrumentation and Measurement Technology Conference

- (I2MTC), pp 1–6. doi:10.1109/I2MTC43012.2020.9128927. ISSN: 2642-2077
- Cho, Y., Yumoto, K., Yabe, Y., Mori, S., Ogura, J.A., Yada, T., Miyazaki, A., Yogata, K., Hatakeyama, K., Nishimura, M., Abe, M., Usui, T., Sugita, S. (2022) Development of a multispectral stereo-camera system comparable to Hayabusa2 optical navigation camera (ONC-T) for observing samples returned from asteroid (162173) Ryugu. *Planetary and Space Science* 221, 105549. doi:10.1016/j.pss.2022.105549
- Cloutis, E.A. (2015) The University of Winnipeg's Planetary Spectrophotometer Facility (aka HOSERLab): What's New. In: 46th Lunar and Planetary Science Conference. 1187. Lunar and Planetary Institute, The Woodlands, TX, US
- Cloutis, E.A., Hudon, P., Hiroi, T., Gaffey, M.J., Mann, P. (2011) Spectral reflectance properties of carbonaceous chondrites: 2. CM chondrites. *Icarus* 216(1), 309–346. doi:10.1016/j.icarus.2011.09.009
- Cloutis, E., Craig, M., Kaletzke, L., McCormack, K., Stewart, L. (2006) HOSERLab: A New Planetary Spectrophotometer Facility. In: 37th Lunar and Planetary Science Conference. 2121. Lunar and Planetary Institute, The Woodlands, TX, US
- Fraeman, A.A., Arvidson, R.E., Murchie, S.L., Rivkin, A., Bibring, J.-P., Choo, T.H., Gondet, B., Humm, D., Kuzmin, R.O., Manaud, N., Zabalueva, E.V. (2012) Analysis of disk-resolved OMEGA and CRISM spectral observations of Phobos and Deimos. *Journal of Geophysical Research: Planets* 117(E11). doi:10.1029/2012JE004137
- Fraeman, A.A., Murchie, S.L., Arvidson, R.E., Clark, R.N., Morris, R.V., Rivkin, A.S., Vilas, F. (2014) Spectral absorptions on Phobos and Deimos in the visible/near infrared wavelengths and their compositional constraints. *Icarus* 229, 196–205. doi:10.1016/j.icarus.2013.11.021
- Furukawa, Y., Ponce, J. (2010) Combining Multi-view Stereo and Bundle Adjustment for Accurate Camera Calibration. In: Ronfard, R., Taubin, G. (eds.) *Image and Geometry Processing for 3-D Cinematography. Geometry and Computing*. Springer, Berlin, Heidelberg, pp 151–169
- Grøtte, M.E., Birkeland, R., Honoré-Livermore, E., Bakken, S., Garrett, J.L., Prentice, E.F., Sigernes, F., Orlandić, M., Gravdahl, J.T., Johansen, T.A. (2022) Ocean Color Hyperspectral Remote Sensing With High Resolution and Low Latency—The HYPSO-1 CubeSat Mission. *IEEE Transactions on Geoscience and Remote Sensing* 60, 1–19. doi:10.1109/TGRS.2021.3080175. Conference Name: IEEE Transactions on Geoscience and Remote Sensing
- Hamilton, V.E., Keller, L.P., Haeneccour, P., Barnes, J.J., Hill, D., H. C. Connolly, J., Lauretta, D.S. (2024) Mineralogy of Bennu From Spectral Analysis of the Sample Returned By OSIRIS-REx. In: 55th Lunar and Planetary Science Conference. 1366. Lunar and Planetary Institute, Woodlands, TX, US
- Harris, J.K., Cousins, C.R., Gunn, M., Grindrod, P.M., Barnes, D., Crawford, I.A., Cross, R.E., Coates, A.J. (2015) Remote detection of past habitability at Mars-analogue hydrothermal alteration terrains using an ExoMars Panoramic Camera emulator. *Icarus* 252, 284–300. doi:10.1016/j.icarus.2015.02.004
- Janesick, J., Klaasen, K., Elliott, T. (1985) CCD Charge Collection Efficiency And The Photon Transfer Technique. In: *Proceedings Solid-State Imaging Arrays*, vol 0570. International Society for Optics and Photonics, San Diego, US, pp 7–19. doi:10.1117/12.950297
- Janesick, J.R. (2007) Photon Transfer: DN to [lambda]. SPIE, Bellingham, Washington, US
- Jähne, B EMVA Standard 1288: Standard for Characterisation of Image Sensors and Cameras. European Machine Vision Association. Release 3.1. <https://www.emva.org/wp-content/uploads/EMVA1288-3.1a.pdf> Accessed 2019-07-15
- Kameda, S., Suzuki, H., Cho, Y., Koga, S., Yamada, M., Nakamura, T., Hiroi, T., Sawada, H., Honda, R., Morota, T., Honda, C., Takei, A., Takamatsu, T., Okumura, Y., Sato, M., Yasuda, T., Shibasaki, K., Ikezawa, S., Sugita, S. (2015) Detectability of hydrous minerals using ONC-T camera onboard the Hayabusa2 spacecraft. *Advances in Space Research* 56(7), 1519–1524. doi:10.1016/j.asr.2015.06.037
- Kameda, S., Suzuki, H., Takamatsu, T., Cho, Y., Yasuda, T., Yamada, M., Sawada, H., Honda, R., Morota, T., Honda, C., Sato, M., Okumura, Y., Shibasaki, K., Ikezawa, S., Sugita, S. (2017) Preflight Calibration Test Results for Optical Navigation Camera Telescope (ONC-T) Onboard the Hayabusa2 Spacecraft. *Space Science Reviews* 208(1), 17–31. doi:10.1007/s11214-015-0227-y
- Kameda, S., Ozaki, M., Enya, K., Fuse, R., Kouyama, T., Sakatani, N., Suzuki, H., Osada, N., Kato, H., Miyamoto, H., Yamazaki, A., Nakamura, T., Okamoto, T., Ishimaru, T., Hong, P., Ishibashi, K., Takashima, T., Ishigami, R., Kuo, C.-L., Abe, S., Goda, Y., Murao, H., Fujishima, S., Aoyama, T., Hagiwara, K., Mizumoto, S., Tanaka, N., Murakami, K., Matsumoto, M., Tanaka, K., Sakuta, H. (2021) Design of telescopic nadir imager for geomorphology (TENGOO) and observation of surface reflectance by optical chromatic imager (OROCHI) for the Martian Moons Exploration (MMX). *Earth, Planets and Space* 73(1), 218. doi:10.1186/s40623-021-01462-9
- Kobayashi, M., Krüger, H., Senshu, H., Wada, K., Okudaira, O., Sasaki, S., Kimura, H. (2018) In situ observations of dust particles in Martian dust belts using a large-sensitive-area dust sensor. *Planetary and Space Science* 156, 41–46. doi:10.1016/j.pss.2017.12.011
- Kowa Optimed Deutschland GmbH. LM12HC 1" 12mm 5MP C-Mount Lens. Datasheet HR976NCN-3H, Kowa Optimed Deutschland GmbH, Fichtenstr. 123, 40233 Duesseldorf, Germany (December 2014). <https://www.kowa-lenses.com/en/lm12hc-5mp-industrial-lens-c-mount> Accessed 2023-07-10
- Kuramoto, K., Kawakatsu, Y., Fujimoto, M., Araya, A., Barucci, M.A., Genda, H., Hirata, N., Ikeda, H., Imamura, T., Helbert, J., Kameda, S., Kobayashi, M., Kusano, H., Lawrence, D.J., Matsumoto, K., Michel, P., Miyamoto, H., Morota, T., Nakagawa, H., Nakamura, T., Ogawa, K., Otake, H., Ozaki, M., Russell, S., Sasaki, S., Sawada, H., Senshu, H., Tachibana, S., Terada, N., Ulamec, S., Usui, T., Wada, K., Watanabe, S.-i., Yokota, S. (2022) Martian moons exploration MMX: sample return mission to Phobos elucidating formation processes of habitable planets. *Earth, Planets and Space* 74(1), 12. doi:10.1186/s40623-021-01545-7
- Lauretta, D.S., Adam, C.D., Allen, A.J., Ballouz, R.-L., Barnouin, O.S., Becker, K.J., Becker, T., Bennett, C.A., Bierhaus, E.B., Bos, B.J., Burns, R.D., Campins, H., Cho, Y., Christensen, P.R., Church, E.C.A., Clark, B.E., Connolly, H.C., Daly, M.G., DellaGiustina, D.N., Drouet d'Aubigny, C.Y., Emery, J.P., Enos, H.L., Kasper, S.F., Garvin, J.B., Getzandanner, K., Golish, D.R., Hamilton, V.E., Hergenrother, C.W., Kaplan, H.H., Keller, L.P., Lessac-Chenen, E.J., Liounis, A.J., Ma, H., McCarthy, L.K., Miller, B.D., Moreau, M.C., Morota, T., Nelson, D.S., Nolau, J.O., Olds, R., Pajola, M., Peigrift, J.Y., Polit, A.T., Ravine, M.A., Reuter, D.C., Rizk, B., Rozitis, B., Ryan, A.J., Sahr, E.M., Sakatani, N., Seabrook, J.A., Selznick, S.H., Skeen, M.A., Simon, A.A., Sugita, S., Walsh, K.J., Westermann, M.M., Wolner, C.W.V., Yumoto, K. (2022) Spacecraft sample collection and subsurface excavation of asteroid (101955) Bennu. *Science* 377(6603), 285–291. doi:10.1126/science.abm1018
- Lawrence, D.J., Peplowski, P.N., Beck, A.W., Burks, M.T., Chabot, N.L., Cully, M.J., Elphic, R.C., Ernst, C.M., Fix, S., Goldsten, J.O., Hoffer, E.M., Kusano, H., Murchie, S.L., Schratz, B.C., Usui, T., Yokley, Z.W. (2019) Measuring the Elemental Composition of Phobos: The Mars-moon Exploration with GAMMA rays and NEutrons (MEGANE) Investigation for the Martian Moons eXploration (MMX) Mission. *Earth and Space Science* 6(12), 2019–000811. doi:10.1029/2019EA000811. eprint: <https://onlinelibrary.wiley.com/doi/pdf/10.1029/2019EA000811>
- Maki, J.N., Bell, J.F., Herkenhoff, K.E., Squyres, S.W., Kiely, A., Klimesh, M., Schwochert, M., Litwin, T., Willson, R., Johnson, A., Maimone, M., Baumgartner, E., Collins, A., Wadsworth, M., Elliot, S.T., Dingizian, A., Brown, D., Hagerott, E.C., Scherr, L., Deen, R., Alexander, D., Lorre, J. (2003) Mars Exploration Rover Engineering Cameras. *Journal of Geophysical Research: Planets* 108(E12). doi:10.1029/2003JE002077
- Martin, P.E., Ehlmann, B.L., Thomas, N.H., Wiens, R.C., Hollis, J.J.R., Beegle, L.W., Bhartia, R., Clegg, S.M., Blaney, D.L. (2020) Studies of a Lacustrine-Volcanic Mars Analog Field Site With Mars-2020-Like Instruments. *Earth and Space Science* 7(2),

- 2019–000720. doi:10.1029/2019EA000720
- Michel, P., Ulamec, S., Böttger, U., Grott, M., Murdoch, N., Vernazza, P., Sunday, C., Zhang, Y., Valette, R., Castellani, R., Biele, J., Tardivel, S., Groussin, O., Jorda, L., Knollenberg, J., Grundmann, J.T., Arrat, D., Pont, G., Mary, S., Grebenstein, M., Miyamoto, H., Nakamura, T., Wada, K., Yoshikawa, K., Kuramoto, K. (2022) The MMX rover: performing in situ surface investigations on Phobos. *Earth, Planets and Space* 74(1), 2. doi:10.1186/s40623-021-01464-7
- Nakamura, T., Matsumoto, M., Amano, K., Enokido, Y., Zolensky, M.E., Mikouchi, T., Genda, H., Tanaka, S., Zolotov, M.Y., Kurosawa, K., Wakita, S., Hyodo, R., Nagano, H., Nakashima, D., Takahashi, Y., Fujioka, Y., Kikui, M., Kagawa, E., Matsuoka, M., Brearley, A.J., Tsuchiyama, A., Sugita, S., Hiroi, T., Kitazato, K., Brownlee, D., Joswiak, D.J., Takahashi, M., Ninomiya, K., Takahashi, T., Osawa, T., Terada, K., Brenker, F.E., Tkalcic, B.J., Vincze, L., Brunetto, R., Aléon-Toppani, A., Chan, Q.H.S., Roskosz, M., Viennet, J-C., Beck, P., Alp, E.E., Michikami, T., Nagaishi, Y., Tsuji, T., Ino, Y., Martinez, J., Han, J., Dolocan, A., Bodnar, R.J., Tanaka, M., Yoshida, H., Sugiyama, K., King, A.J., Fukushi, K., Suga, H., Yamashita, S., Kawai, T., Inoue, K., Nakato, A., Noguchi, T., Vilas, F., Hendrix, A.R., Jarramillo-Correa, C., Domingue, D.L., Dominguez, G., Gainsforth, Z., Engrand, C., Duprat, J., Russell, S.S., Bonato, E., Ma, C., Kawamoto, T., Wada, T., Watanabe, S., Endo, R., Enju, S., Liu, L., Rubino, S., Tack, P., Takeshita, S., Takeichi, Y., Takeuchi, A., Takigawa, A., Takir, D., Tanigaki, T., Taniguchi, A., Tsukamoto, K., Yagi, T., Yamada, S., Yamamoto, K., Yamashita, Y., Yasutake, M., Uesugi, K., Umegaki, I., Chiu, I., Ishizaki, T., Okumura, S., Palomba, E., Pilorget, C., Potin, S.M., Alasli, A., Anada, S., Araki, Y., Sakatani, N., Schultz, C., Sekizawa, O., Sitzman, S.D., Sugiura, K., Sun, M., Dartois, E., De Pauw, E., Dionnet, Z., Djouadi, Z., Falkenberg, G., Fujita, R., Fukuma, T., Gearba, I.R., Hagiya, K., Hu, M.Y., Kato, T., Kawamura, T., Kimura, M., Kubo, M.K., Langenhorst, F., Lantz, C., Lavina, B., Lindner, M., Zhao, J., Vekemans, B., Baklouti, D., Bazi, B., Borondics, F., Nagasawa, S., Nishiyama, G., Nitta, K., Mathurin, J., Matsumoto, T., Mitsukawa, I., Miura, H., Miyake, A., Miyake, Y., Yurimoto, H., Okazaki, R., Yabuta, H., Naraoka, H., Sakamoto, K., Tachibana, S., Connolly, H.C., Lauretta, D.S., Yoshitake, M., Yoshikawa, M., Yoshikawa, K., Yoshihara, K., Yokota, Y., Yogata, K., Yano, H., Yamamoto, Y., Yamamoto, D., Yamada, M., Yamada, T., Yada, T., Wada, K., Usui, T., Tsukizaki, R., Terui, F., Takeuchi, H., Takei, Y., Iwamae, A., Soejima, H., Shirai, K., Shimaki, Y., Senshu, H., Sawada, H., Saiki, T., Ozaki, M., Ono, G., Okada, T., Ogawa, N., Ogawa, K., Noguchi, R., Noda, H., Nishimura, M., Namiki, N., Nakazawa, S., Morota, T., Miyazaki, A., Miura, A., Mimasu, Y., Matsumoto, K., Kumagai, K., Kouyama, T., Kikuchi, S., Kawahara, K., Kameda, S., Iwata, T., Ishihara, Y., Ishiguro, M., Ikeda, H., Hosoda, S., Honda, R., Honda, C., Hitomi, Y., Hirata, N., Hirata, N., Hayashi, T., Hayakawa, M., Hatakeyama, K., Furuya, S., Fukai, R., Fujii, A., Cho, Y., Arakawa, M., Abe, M., Watanabe, S., Tsuda, Y. (2022) Formation and evolution of carbonaceous asteroid Ryugu: Direct evidence from returned samples. *Science* 379(6634), 8671. doi:10.1126/science.abn8671. Accessed 2024-07-17
- Ogohara, K., Nakagawa, H., Aoki, S., Kouyama, T., Usui, T., Terada, N., Imamura, T., Montmessin, F., Brain, D., Doressoundiram, A., Gautier, T., Hara, T., Harada, Y., Ikeda, H., Koike, M., Leblanc, F., Ramirez, R., Sawyer, E., Seki, K., Spiga, A., Vandaele, A.C., Yokota, S., Barucci, A., Kameda, S. (2022) The Mars system revealed by the Martian Moons eXploration mission. *Earth, Planets and Space* 74(1), 1. doi:10.1186/s40623-021-01417-0
- OnSemi. KAI-08051/D. Datasheet, Semiconductor Components Industries, LLC (December 2015). <https://www.onsemi.com/download/data-sheet/pdf/kai-08051-d.pdf> Accessed 2022-04-05
- Senshu, H., Mizuno, T., Umetani, K., Nakura, T., Konishi, A., Ogawa, A., Ikeda, H., Matsumoto, K., Noda, H., Ishihara, Y., Sasaki, S., Tateno, N., Ikuse, Y., Mayuzumi, K., Kase, T., Kashine, H. (2021) Light detection and ranging (LIDAR) laser altimeter for the Martian Moons Exploration (MMX) spacecraft. *Earth, Planets and Space* 73(1), 219. doi:10.1186/s40623-021-01537-7
- Shaw, A., Daly, M.G., Cloutis, E., Basic, G., Hamilton, D., Tait, K., Hyde, B., Lymer, E., Balachandran, K. (2016) Reflectance properties of grey-scale Spectralon® as a function of viewing angle, wavelength, and polarization. *International Journal of Remote Sensing* 37(11), 2510–2523. doi:10.1080/01431161.2016.1182664
- Sony Corporation Datasheet for Sony IMX249LLJ CMOS Sensor. Datasheet, Sony Corporation (February 2015). https://s1-d1.theimagingsource.com/api/2.5/packages/publication/sensor-sony/imx249llj/6a48775d-a298-532c-b1ec-5b4c0262b7c4/imx249llj_1.0.en-US.pdf Accessed 2023-07-05
- St. Clair, M., Million, C. Western Washington University Visible-Infrared Spectral Browser: VISOR. Western Washington University. <https://zenodo.org/doi/10.5281/zenodo.6604832>. <https://westernreflectancelab.com/visor/>
- The Imaging Source Europe GmbH. DMK 33GX249 Technical Reference Manual. Technical report, The Imaging Source Europe GmbH., Bremen, Germany (April 2019). <https://s1-d1.theimagingsource.com/api/2.5/packages/documentation/manual-trm/trmdmk33gx249/4e35f210-d317-530c-92a2-292d0d9c65cd/trmdmk33gx249.en-US.pdf> Accessed 2023-06-05
- van den Bergh, F. MTF mapper. <https://sourceforge.net/projects/mtfmapper/> Accessed 2023-07-10 07
- Yokota, S., Terada, N., Matsuoka, A., Murata, N., Saito, Y., Delcourt, D., Futaana, Y., Seki, K., Schaible, M.J., Asamura, K., Kasahara, S., Nakagawa, H., Nishino, M.N., Nomura, R., Keika, K., Harada, Y., Imajo, S. (2021) In situ observations of ions and magnetic field around Phobos: the mass spectrum analyzer (MSA) for the Martian Moons eXploration (MMX) mission. *Earth, Planets and Space* 73(1), 216. doi:10.1186/s40623-021-01452-x
- Yumoto, K., Tatsumi, E., Kouyama, T., Golish, D.R., Cho, Y., Morota, T., Kameda, S., Sato, H., Rizk, B., DellaGiustina, D.N., Yokota, Y., Suzuki, H., de León, J., Campins, H., Licandro, J., Popescu, M., Rizos, J.L., Honda, R., Yamada, M., Sakatani, N., Honda, C., Matsuoka, M., Hayakawa, M., Sawada, H., Ogawa, K., Yamamoto, Y., Lauretta, D.S., Sugita, S. (2024) Comparison of optical spectra between asteroids Ryugu and Bennu: II. High-precision analysis for space weathering trends. *Icarus* 420, 116204. doi:10.1016/j.icarus.2024.116204

Figure Legends

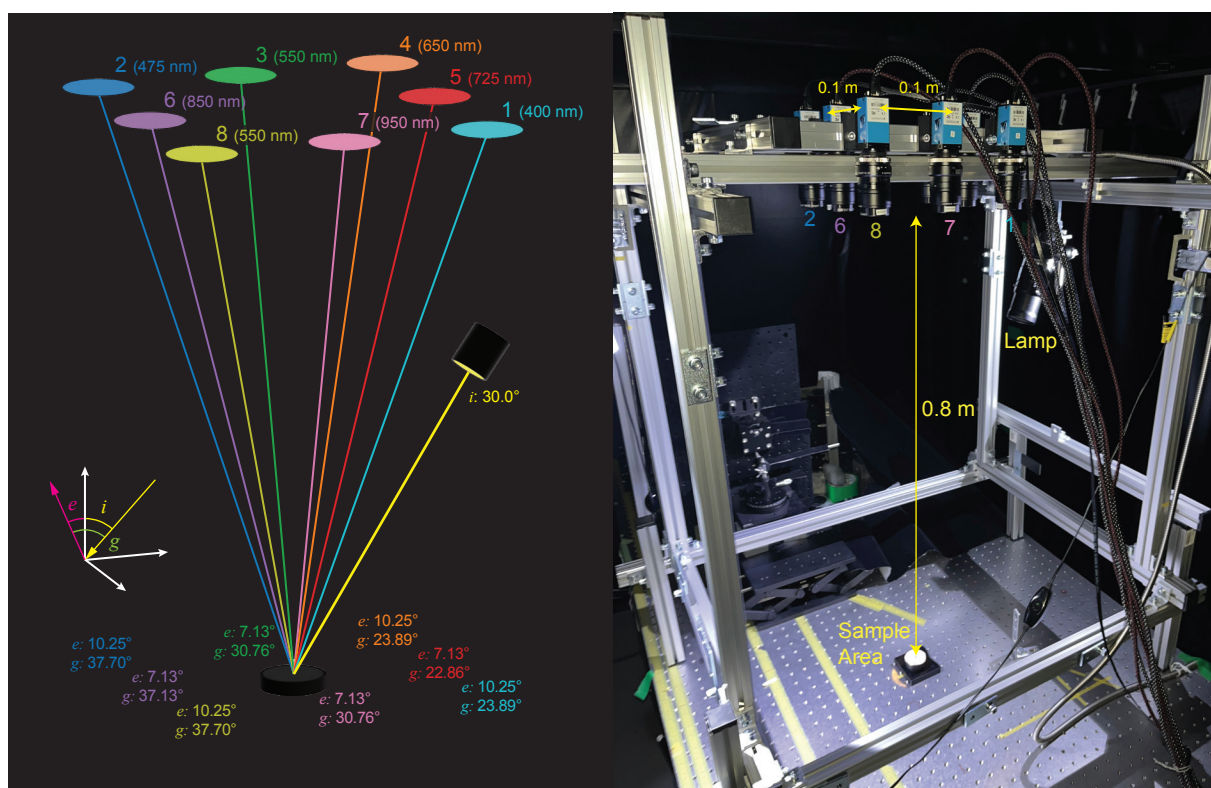


Figure 1 The observation geometry (left) of the Laboratory OROCHI Simulator (LOROS) (right). The annotated diagram (left) shows the centre wavelength of each channel, and the incidence (*i*), emergence (*e*) and phase (*g*) angles, matching the planned configuration of the OROCHI Flight Model. The annotated image (right) shows the arrangement of the 8 DMK 33GX249 cameras on the aluminium supporting frame, the illumination lamp, and the Spectralon™ 99% reflectance target (SCT99) in the sample area.

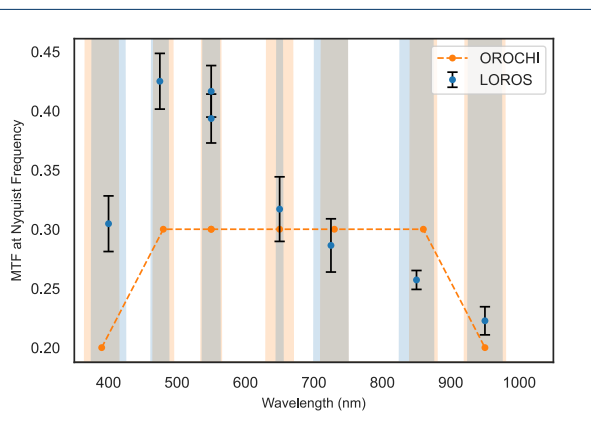


Figure 2 Modulation Transfer Function (MTF) of LOROS vs OROCHI. Observed MTF of LOROS spectral channels (blue markers) at the LOROS sensor Nyquist frequency, derived from the line-spread function measured from a slant-edge target, in comparison to the required MTF of OROCHI (orange markers) at the OROCHI sensor Nyquist frequency, as specified by Kameda et al. (2021).

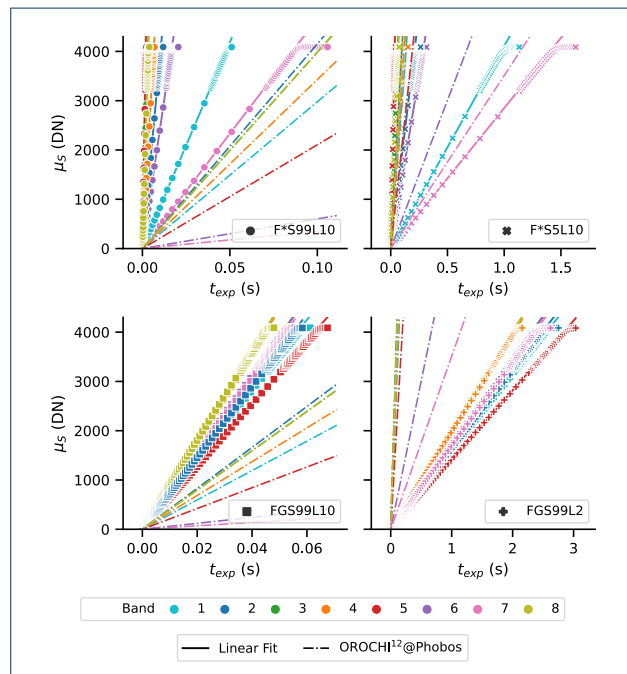


Figure 3 Mean pixel signal vs exposure time for each camera under various illumination conditions. Mean signal measured over a 28×28 pixel uniformly illuminated area of the SCT99 (S99) and SCT5 (S5) Spectralon™ reference calibration target, using the designated filter for each channel (F^*) and the same 550 nm filter for each channel (FG), and at arbitrary lamp brightness settings of 10 (L10) and 2 (L2), with configuration denoted by the legend code of each subplot. Solid lines show the linear fits of the response of each channel, and dash-dot lines show the expected digital flux for OROCHI¹² at Phobos.

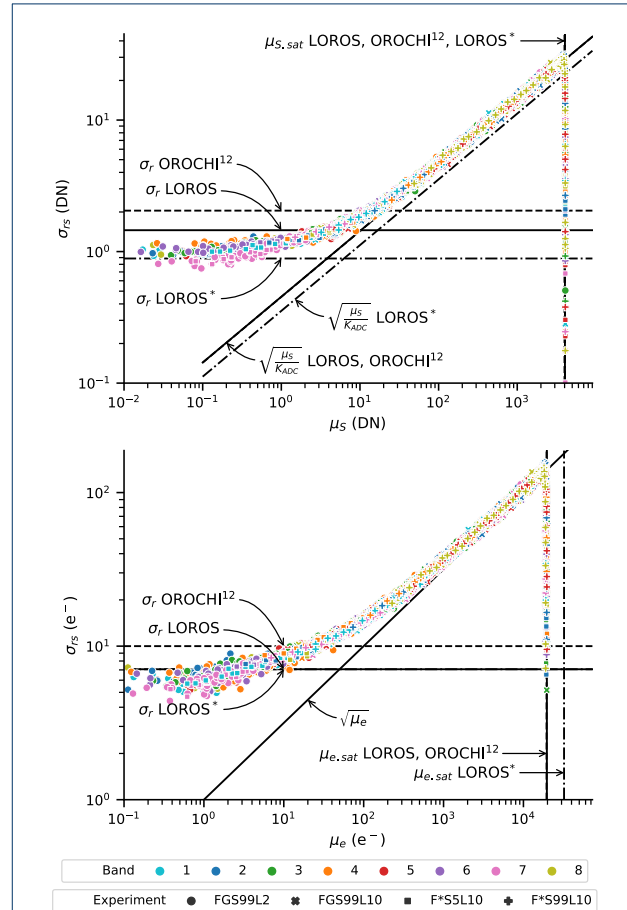
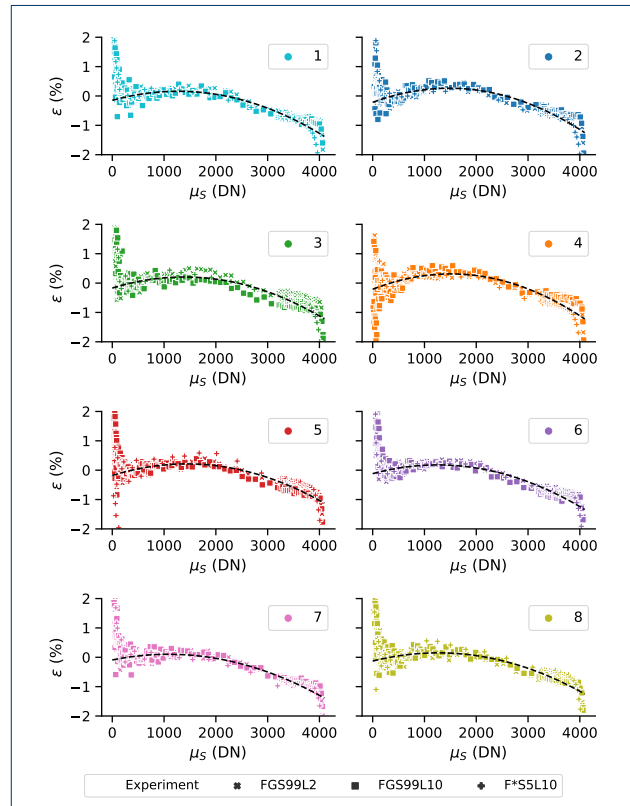
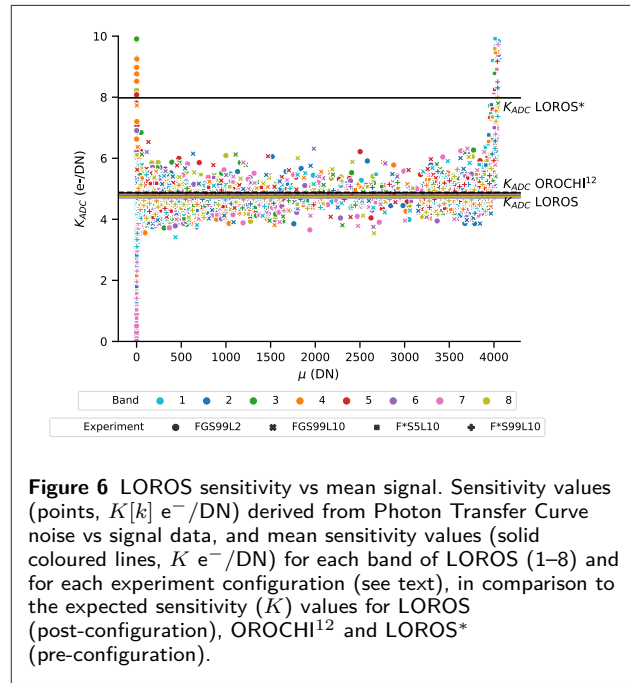
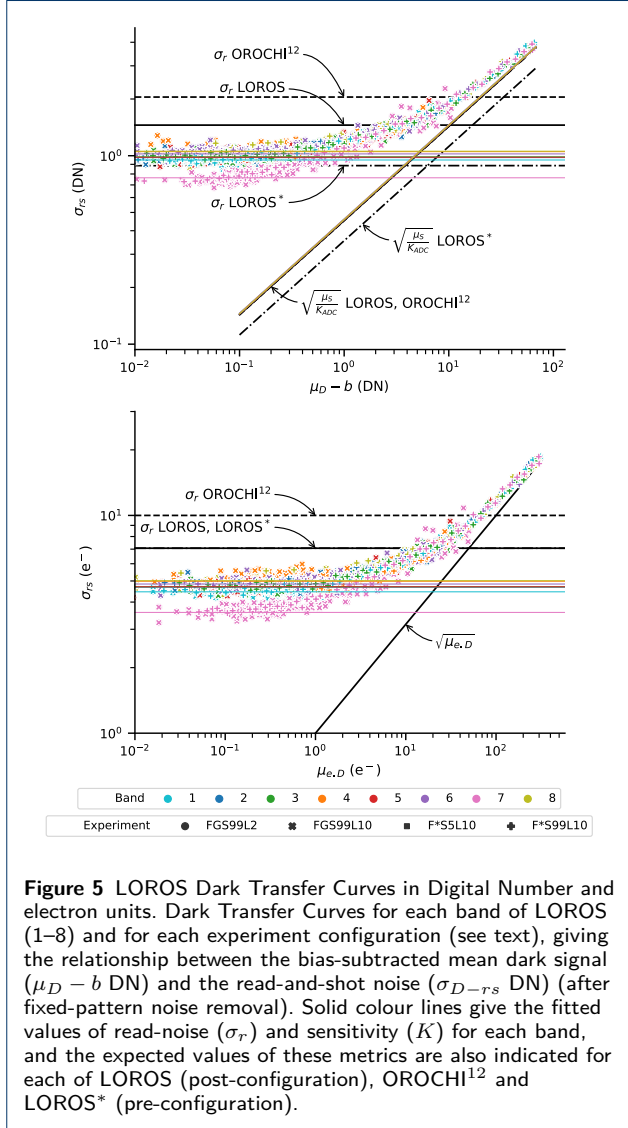


Figure 4 LOROS Photon Transfer Curves in Digital Number and electron units. Photon Transfer Curves for each band of LOROS (1–8) and for each experiment configuration (see text), giving the relationship between the mean signal across the uniformly illuminated 28×28 pixel area (μ_s DN) and the read-and-shot noise (σ_{rs} DN) (after removal of fixed-pattern noise), with the expected key metrics of read-noise (σ_r), saturation capacity ($\mu_{s,sat}$) and sensitivity (K) indicated for each of LOROS (post-configuration), OROCHI¹² and LOROS* (pre-configuration).



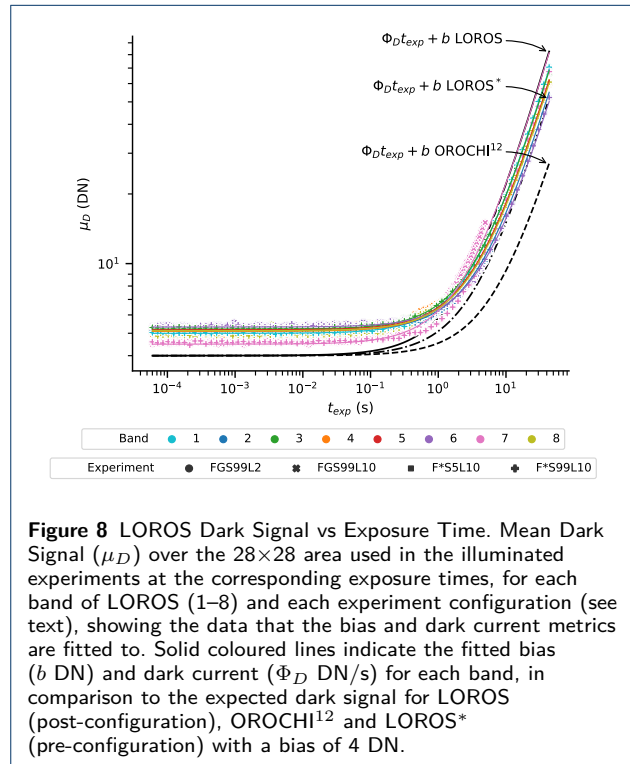


Figure 8 LOROS Dark Signal vs Exposure Time. Mean Dark Signal (μ_D) over the 28×28 area used in the illuminated experiments at the corresponding exposure times, for each band of LOROS (1–8) and each experiment configuration (see text), showing the data that the bias and dark current metrics are fitted to. Solid coloured lines indicate the fitted bias (b DN) and dark current (Φ_D DN/s) for each band, in comparison to the expected dark signal for LOROS (post-configuration), OROCHI¹² and LOROS* (pre-configuration) with a bias of 4 DN.

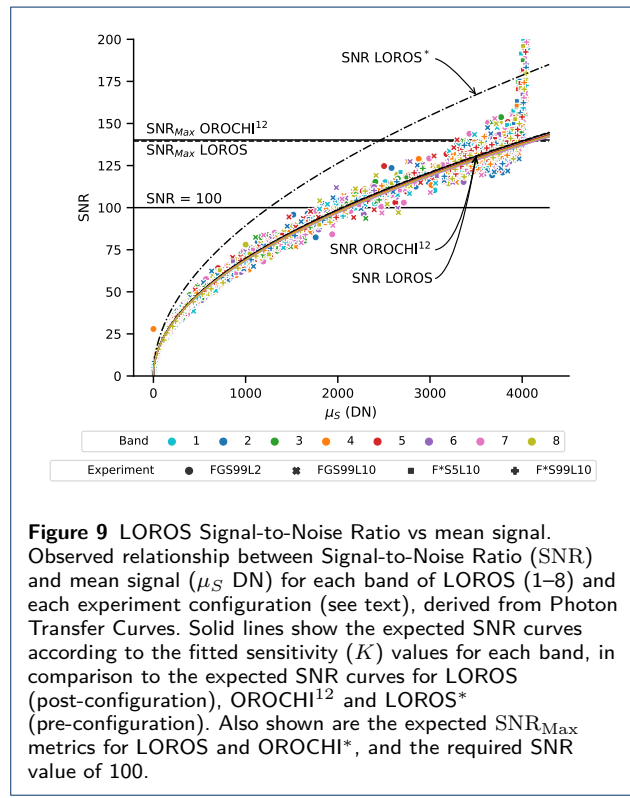


Figure 9 LOROS Signal-to-Noise Ratio vs mean signal. Observed relationship between Signal-to-Noise Ratio (SNR) and mean signal (μ_S DN) for each band of LOROS (1–8) and each experiment configuration (see text), derived from Photon Transfer Curves. Solid lines show the expected SNR curves according to the fitted sensitivity (K) values for each band, in comparison to the expected SNR curves for LOROS (post-configuration), OROCHI¹² and LOROS* (pre-configuration). Also shown are the expected SNR_{Max} metrics for LOROS and OROCHI*, and the required SNR value of 100.

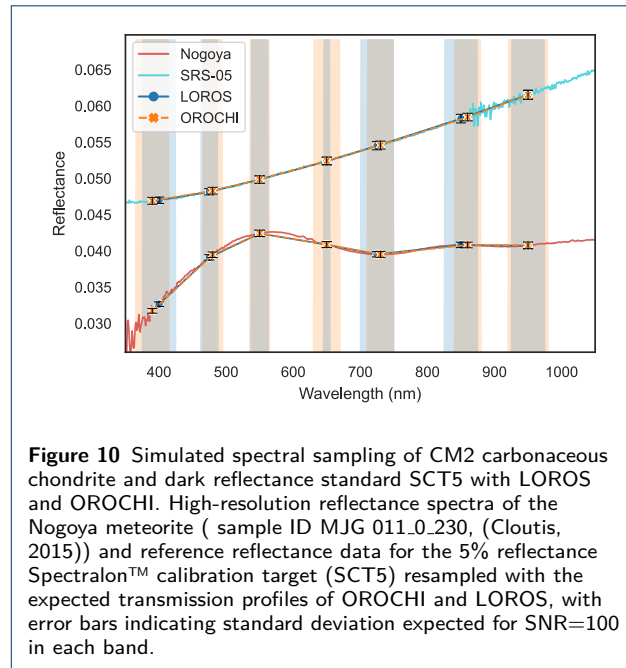


Figure 10 Simulated spectral sampling of CM2 carbonaceous chondrite and dark reflectance standard SCT5 with LOROS and OROCHI. High-resolution reflectance spectra of the Nogoya meteorite (sample ID MJG 011.0_230, (Cloutis, 2015)) and reference reflectance data for the 5% reflectance Spectralon™ calibration target (SCT5) resampled with the expected transmission profiles of OROCHI and LOROS, with error bars indicating standard deviation expected for SNR=100 in each band.

